ELSEVIER

1/32° real-time global ocean prediction and value-added over 1/16° resolution

J.F. Shriver [a],*, H.E. Hurlburt [a], O.M. Smedstad [b], A.J. Wallcraft [a], R.C. Rhodes [a]

[a] *Naval Research Laboratory, Stennis Space Center, MS 39529, USA*
[b] *Planning Systems, Inc., Stennis Space Center, MS 39529, USA*

Abstract

A 1/32° global ocean nowcast/forecast system has been developed by the Naval Research Laboratory at the Stennis Space Center. It started running at the Naval Oceanographic Office in near real-time on 1 Nov. 2003 and has been running daily in real-time since 1 Mar. 2005. It became an operational system on 6 March 2006, replacing the existing 1/16° system which ceased operation on 12 March 2006. Both systems use the NRL Layered Ocean Model (NLOM) with assimilation of sea surface height from satellite altimeters and sea surface temperature from multi-channel satellite infrared radiometers. Real-time and archived results are available online at http://www.ocean.nrlssc.navy.mil/global_nlom. The 1/32° system has improvements over the earlier system that can be grouped into two categories: (1) better resolution and representation of dynamical processes and (2) design modifications. The design modifications are the result of accrued knowledge since the development of the earlier 1/16° system. The improved horizontal resolution of the 1/32° system has significant dynamical benefits which increase the ability of the model to accurately nowcast and skillfully forecast. At the finer resolution, current pathways and their transports become more accurate, the sea surface height (SSH) variability increases and becomes more realistic and even the global ocean circulation experiences some changes (including inter-basin exchange). These improvements make the 1/32° system a better dynamical interpolator of assimilated satellite altimeter track data, using a one-day model forecast as the first guess. The result is quantitatively more accurate nowcasts, as is illustrated by several model-data comparisons. Based on comparisons with ocean color imagery in the northwestern Arabian Sea and the Gulf of Oman, the 1/32° system has even demonstrated the ability to map small eddies, 25–75 km in diameter, with 70% reliability and a median eddy center location error of 22.5 km, a surprising and unanticipated result from assimilation of altimeter track data. For all of the eddies (50% small eddies), the reliability was 80% and the median eddy center location error was 29 km. The 1/32° system also exhibits improved forecast skill in relation to the 1/16° system. This is due to (a) a more accurate initial condition for the forecast and (b) better resolution and representation of critical dynamical processes (such as upper ocean – topographic coupling via mesoscale flow instabilities) which allow the model to more accurately evolve these features in time while running in forecast mode (forecast atmospheric forcing for the first 5 days, then gradually reverting toward climatology for the remainder of the 30-day forecast period). At 1/32° resolution, forecast SSH generally compares better with unassimilated observations and the anomaly correlation of the forecast SSH exceeds that from persistence by a larger amount than found in the 1/16° system.
Published by Elsevier B.V.

Keywords: Global ocean prediction; Prediction of mesoscale variability; Data assimilation; Ocean forecast verification

---

* Corresponding author.
 E-mail address: shriver@nrlssc.navy.mil (J.F. Shriver).

1. Introduction

The development of a data-assimilative 1/32° global ocean nowcast/forecast system is the culmination of a long-standing effort, which includes the associated basic research and exploratory development. For operational purposes, the U.S. Navy niche in ocean modeling and prediction is high horizontal resolution. For global and basin-scales that means, for example, the ocean models must have sufficient resolution to (1) depict narrow oceanic current systems and their meandering, (2) represent sharp ocean fronts and eddies, (3) represent geometric and topographic features such as narrow passages and islands, (4) simulate upper ocean – topographic coupling via flow instabilities that is strong enough to accurately depict the pathways of many current systems in the world ocean and (5) provide boundary conditions for even higher resolution coastal models.

How much resolution is enough? Dramatic improvements are found as the grid resolution is increased up to 1/32° (∼ 3.5 km at mid-latitudes), but only modest changes are found when the resolution is increased to 1/64° (Hurlburt and Hogan, 2000). A similar result was found in the Japan/East Sea (Hogan and Hurlburt, 2000). As the resolution is increased, the pathways of current systems become much more accurate, ocean fronts become sharper and extend much farther to the east across major ocean basins, eddies fill the entire model domain, the large-scale shape of basin-scale ocean gyres is altered, and the global ocean circulation is changed, including inter-basin exchanges, and the pathways of global scale currents and their transports. One of the key aspects of model dynamics that drives the resolution requirement is the need to resolve the vorticity dynamics of baroclinic instability, not just the resulting mesoscale eddies. This is particularly evident when studying the impact of ocean model resolution on upper ocean – topographic coupling via mesoscale flow instabilities. Baroclinic instability is very effective in transferring energy from the upper ocean to the abyssal ocean and is a critical mechanism in driving many deep mean flows (as well as time varying flows) (Holland and Lin, 1975; Holland, 1978; Rhines and Holland, 1979; and other references in this paragraph). In ocean models the energy transfer and resulting abyssal currents increase greatly up to ∼ 1/32° resolution. In turn abyssal currents at mid and high latitudes can be very effective in steering upper ocean currents and improving simulations of their pathways (Hurlburt and Thompson, 1980; Hurlburt et al., 1996; Hurlburt and Metzger, 1998; Hogan and Hurlburt, 2000; Tilburg et al., 2001; Hogan and Hurlburt, 2005). From all of the preceding discussion, the 1/32° model

should have improved dynamical interpolation skill when assimilating data, and it should demonstrate improved forecast skill. However, the preceding results indicate that increases in grid resolution beyond 1/32° will yield only modest improvements in most deep-water regions of the World Ocean (much higher resolution is needed in coastal regions). Hence, our target resolution globally is 1/32°. In relation to the size of ocean eddies, 1/32° (∼ 3.5 km mid-latitude) resolution for the ocean is similar to the resolution currently used by most weather forecasting models in relation to the size of atmospheric highs and lows, and in relation to the corresponding first internal mode radii of deformation for the ocean and the atmosphere.

Applications for ocean nowcast/forecast systems include assimilation and synthesis of global satellite surface data; ocean prediction; optimum track ship routing; search and rescue; anti-submarine warfare and surveillance; tactical planning; high resolution boundary conditions that are essential for even higher resolution coastal models; sea surface temperature for long range weather prediction; inputs to ice models, biochemical models and shipboard environmental products; environmental simulation and synthetic environments; observing system simulation and assessment; ocean research and education; pollution and tracer tracking; fisheries and marine resource management; impact on ocean structures such as oil rigs, and inputs to water quality assessment. Data-assimilative eddy–resolving ocean prediction systems can be very effective in using real-time satellite altimeter data to map and forecast the "ocean weather" (e.g. ocean eddies and the meandering currents and fronts) as demonstrated in earlier studies (e.g. Hurlburt et al., 2000; Smedstad et al., 2003). Sea surface temperature is assimilated as well.

Here we discuss the operational 1/32° near-global NLOM nowcast/forecast system and the value added of the resolution increase over the earlier 1/16° system discussed in Smedstad et al. (2003). The 1/16° system has been running continuously in real-time at the Naval Oceanographic Office (NAVOCEANO), Stennis Space Center, MS, since 18 Oct. 2000 and it became an operational system on 27 Sept. 2001. The 1/32° system has been running in near real-time since 1 Nov. 2003 and daily in real-time since 1 Mar. 2005. It became an operational system on 6 March 2006, replacing the existing 1/16° system which ceased operation on 12 March 2006. Results from both systems are available online at http://www.ocean.nrlssc.navy.mil/global_nlom. Both systems use the NRL Layered Ocean Model (NLOM) with assimilation of sea surface height from satellite altimeters and sea surface temperature from multi-channel

satellite infrared radiometers. The next section gives an overview of this system. Improvements in the nowcast accuracy and forecast skill of the 1/32° over the 1/16° system are discussed in Section 3, and the conclusions are summarized in Section 4.

2. The nowcast/forecast system

2.1. The NRL layered ocean model (NLOM)

The model component of the ocean prediction system is based on the primitive equation model of Hurlburt and Thompson (1980) but with greatly expanded capability (Wallcraft, 1991; Wallcraft and Moore, 1997; Moore and Wallcraft, 1998; Wallcraft et al., 2003). The model has a nearly global domain that extends from 72°S to 65°N. The horizontal resolution of each model variable is 1/32° in latitude by 45/1024° in longitude or ~ 3.5 km at mid-latitudes, which is eddy-resolving. It has 6 dynamical layers plus the mixed layer and vertically compressed but otherwise realistic bottom topography that is confined to the lowest layer of the model, except that flows through straits are constrained to small values below the sill depth. The model has lateral boundaries that follow the 200-m isobath with a few exceptions, such as the shallow straits around the Japan/East Sea. At the solid boundaries kinematic and no-slip boundary conditions are used. Much of the deep-water formation in the far North Atlantic is parameterized via observationally based flows through northern boundary ports at the Davis Strait and the three straits between southern Greenland and Scotland.

In the model, the prognostic variables are layer density, layer thickness, layer volume transport per unit width (layer velocity times layer thickness), sea surface temperature (SST) and mixed layer depth (MLD). The model has a free surface, corresponding to sea surface height (SSH) (i.e., a variable observed by satellite altimetry). The Kraus–Turner type mixed layer is not confined within the upper dynamical layer. To some extent it is independent of the dynamical layers, but is not entirely passive. In particular, (1) a deep mixed layer can distribute surface forcing across multiple dynamical layers, (2) thermal expansion is based on the mixed layer temperature T_m rather than layer 1 temperature, and (3) surface heat flux depends on T_m. All three factors can change the steric sea surface height anomaly. The embedded mixed layer model used here carries prognostic equations for SST and MLD and is discussed in detail by Wallcraft et al. (2003).

Below the mixed layer, the density of the top 5 dynamical layers is relaxed toward the annual mean climatological density of that layer except for layer 1, which is relaxed toward a monthly mean climatology interpolated to daily values because of the significant seasonal cycle within that layer. The Modular Ocean Data Assimilation System (MODAS) climatology (Fox et al., 2002) is used for this purpose. Unlike other models with fixed levels in the vertical, such relaxation does not significantly damp the anomalies because in NLOM most of the information about circulation anomalies is carried by layer thickness variations, not density variations. For example, NLOM maintained a Rossby wave generated by the 1982–83 El Niño for at least a decade (Jacobs et al., 1994) without oceanic data assimilation except for the relaxation to climatological density within layers.

Additional details concerning NLOM can be found in Hurlburt et al. (1996), Metzger and Hurlburt (1996), and Shriver and Hurlburt (1997). Shriver and Hurlburt (1997) discuss the ability of global NLOM to simulate the global overturning circulation, including the cross-interfacial mixing scheme based on oxygen saturation. Mixing also occurs when there is model layer outcropping. Kara and Hurlburt (2006) discuss NLOM SST simulation skill (with no assimilation of SST data) on time-scales ranging from daily mean values to inter-annual.

2.2. The assimilation scheme

With a model grid the size of the 1/32° NLOM (8192×4608 per layer), it is essential to use an assimilation technique that will not result in a large increase in the model run time. The scheme used is similar to the incremental updating technique described in Smedstad and Fox (1994) and is the same data assimilation scheme used in the current operational 1/16° NLOM system (Smedstad et al., 2003). This technique increases the model run time by about 50% compared to the model running without assimilation. More sophisticated techniques like the ensemble Kalman filter (Evensen, 1994) may increase the run time of the assimilation system by a factor of up to 100.

The SSH data that are assimilated into the model are satellite altimeter SSH deviations from a temporal mean plus the mean SSH described in the next subsection. Currently Jason-1, Geosat-Follow-On (GFO) and Envisat are used in the real-time system. However, data from ERS-2, GFO and Topex/Poseidon were used for the June 2001–May 2002 hindcast results discussed in this paper. In the data assimilation scheme the model SSH is used as a first guess in an OI deviation analysis with a 3-day data window. Anisotropic, spatially varying mesoscale

covariance functions determined from altimeter data (Jacobs et al., 2001) are used in the OI deviation analysis. The surface information is transferred to the deeper layers via the statistical inference technique of Hurlburt et al. (1990). This technique updates the pressure field in all layers below the surface. When the coefficients for the statistical inference were calculated, care was taken to use a recent time window of model fields, namely 1997–2002 at a 15-day interval. A geostrophic velocity correction is calculated from the pressure changes. The velocity correction is not performed between 5° latitude and the equator. Between 5 and 8° the correction is gradually increased to full strength using a hyperbolic tangent function. To further reduce the creation of gravity waves, these corrections are then used incrementally to update the model variables.

The SST assimilation consists of a relaxation of model SST (mixed layer temperature, T_m) toward the MODAS MCSST analysis (T_o). MODAS is an operational system running daily at NAVOCEANO (Fox et al., 2002). The relaxation process is treated as a heat flux where the flux depends on an e-folding time-scale ($r_{sst} = 3$ h during the assimilation) and the mixed layer depth (h_m). In addition, the total heat flux (Q_T from relaxation and the atmosphere (Q_A)) is limited to Q_{min} and Q_{max} of ± 1000 Wm^{-2}, i.e.

$$Q_T = \max(Q_{min}, \min(Q_{max}, Q_A + C_p \rho h_m r_{sst}(T_o - T_m))),$$

where C_p is the specific heat of water and ρ is water density. A benefit of treating the SST assimilation as a heat flux (with a flux limiter) is demonstrated in Zamudio et al. (2002). In that paper 1/16° global NLOM nowcasts show cold SST beneath Hurricane Juliette despite warm MODAS SSTs derived from the surrounding region due to lack of data beneath the cloud cover of the hurricane.

During each 30-day forecast, the forecast SST is relaxed toward climatologically-corrected persistence of the nowcast. In this case the relaxation time-scale is 1/4 the elapsed forecast length (e.g., 1 week for a 4-week forecast). This procedure is used because the atmospheric forecast is only available out to 5 days. During the forecast the model makes the SST look more fluidic and helps keep SST fronts better aligned with currents and SSH fronts than climatologically-corrected persistence. It also helps keep eddies in SSH and SST in phase.

2.3. The mean sea surface height

The mean sea surface height used in the assimilation scheme (Fig. 1) was developed using the same procedures as in Smedstad et al. (2003). It is important to have a mean which has the major ocean currents and associated SSH fronts more sharply defined than is feasible from hydrographic climatologies. As a starting point, the mean SSH from the atmospherically-forced model (with no ocean data assimilation except for the climatological density relaxation) was calculated over the time period of the statistical inference statistics (1997–2002). The accuracy of this mean is substantially enhanced by the climatological density relaxation. The mean was then compared to available sources of information, including mean surface dynamic height over the time period of the satellite observations, mean frontal locations determined from satellite IR, mean SSH determined from nearly simultaneous AXBT underflights of altimeter tracks (Mitchell et al., 1990) and SSH variability from satellite altimeter data. The model mean was then modified via a rubber sheeting technique and other methods designed to operate on SSH fields (Carnes et al., 1996). The Gulf Stream, Gulf of Mexico, Kuroshio, and Japan/East Sea were the only regions where modifications were made.

2.4. The wind and thermal forcing

The wind and thermal forcing used in the 1/32° model are the same as used in the previous 1/16° operational system (Smedstad et al., 2003). The wind stress used is a hybrid of the Fleet Numerical Meteorology and Oceanography Center (FNMOC) Navy Operational Global Atmospheric Prediction System (NOGAPS) (Hogan and Rosmond, 1991; Rosmond et al., 2002) and the Hellerman and Rosenstein (HR) (1983). The long term mean (August 1990–July 1999 for FNMOC) is subtracted from the FNMOC stresses and replaced by the annual mean from HR. From the atmospheric model we get the forcing up to a 5-day forecast. The forcing for the 30-day forecast gradually reverts to climatology beyond 5 days. The last forecast record is weighted with the contemporaneous climatological values with the weight of the forecast decreasing to zero over a 10-day time span. In Section 3.5.3 we discuss the effect of this on ocean forecasts. The thermal forcing also comes from FNMOC NOGAPS. The latent and sensible heat flux formulation is replaced by that of Kara et al. (2002), which makes use of model SST.

Kara et al. (2003) and Kara and Hurlburt (2006) describe experiments showing the ability of NLOM to accurately predict SST over most of the global ocean without relaxation to or assimilation of SST data. These experiments show that NLOM predicts annual mean SST with an RMS error of <0.5 °C for the nearly global model domain in comparison with the Comprehensive Ocean-Atmosphere Data Set (COADS) SST climatology. Using
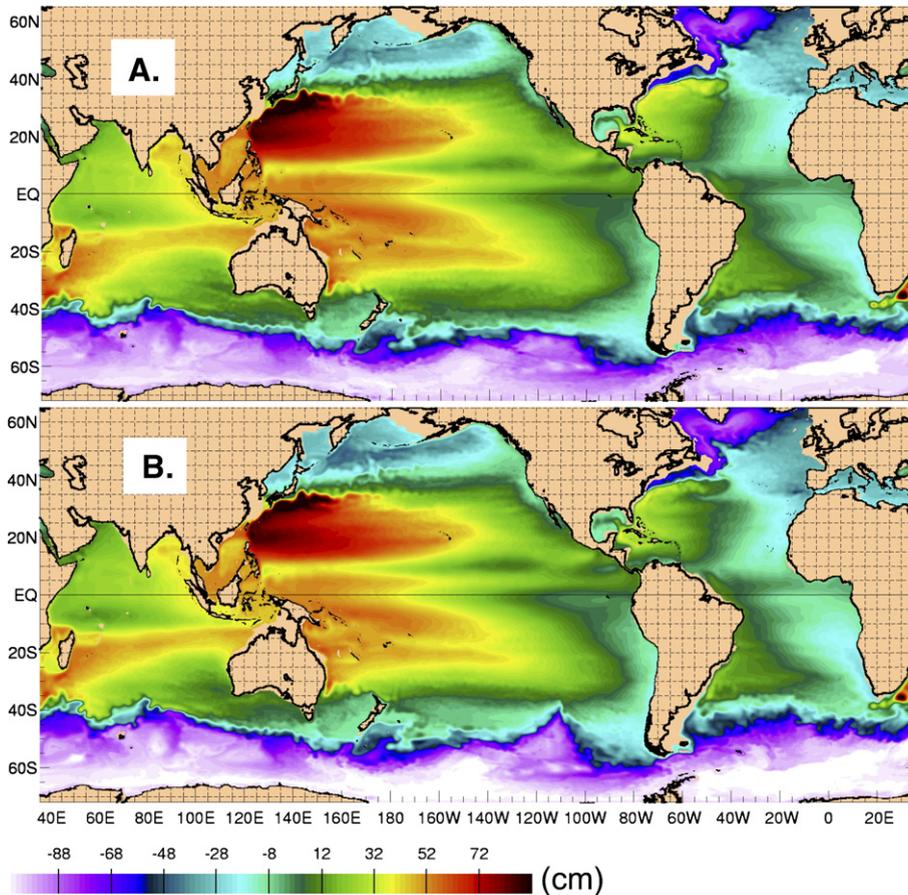
Fig. 1. Slightly modified mean SSH used in the assimilation of satellite altimeter SSH (discussed in Section 2.2) in the (A) 1/32° and (B) 1/16° systems. The 1/32° mean was computed over the time period 1997–2002 and the 1/16° mean was computed over the period 1993–1999. This SSH field is added to the altimeter SSH deviations from a temporal mean.

inter-annual simulations with 6-hourly forcing, Kara and Hurlburt (2006) found that a 1/8° version of the global model gave a median RMS SST error of .6 °C in comparison with 194-year long daily time series (1990–1998) measured at moored buoys in the Pacific from the National Data Buoy Center and the Tropical Atmosphere Ocean (TAO) array (McPhaden, 1995).

2.5. The altimeter and SST data

The real-time altimeter data assimilated into the model are delivered via NAVOCEANO's Altimeter Data Fusion Center. Currently, data from the GFO, Jason-1 and Envisat altimeters are available within 48 h. Better orbit corrections are available with a slightly longer delay. To pick up data with improved orbits and other delayed data, the real-time assimilation cycle restarts 5 days prior to the nowcast time. However, many of the model-data comparisons and the comparisons between the 1/32° and 1/16° global ocean prediction systems use

the period June 2001–May 2002 when altimeter data from ERS-2, GFO and Topex/Poseidon were available. For SST, the model assimilates MODAS SST analyses of satellite MCSST data (in situ SST data are not used). These OI analyses are a daily operational product of NAVOCEANO (Fox et al., 2002).

2.6. The pre-operational cycle

The operational nowcast/forecast system is currently running daily on 316 IBM SP4+ processors at the NAVOCEANO Major Shared Resource Center (MSRC). Each week, the Wednesday nowcast is used to initialize a 30-day model forecast with the atmospheric forcing described in Section 2.4.

3. Results and discussion

The improvements noted in the 1/32° compared to the 1/16° system are attributable to better resolution and

representation of dynamical processes, with some improvement due to design modifications as well. The design modifications are the result of accrued knowledge since the development of the earlier 1/16° system. To illustrate the value added of the 1/32° system over the earlier 1/16° system, several model–data and model–model comparisons are discussed in this section.

3.1. Arabian sea SSH and currents (with and without data assimilation) vs SeaWiFS ocean color

Satellite altimetry provides the key available data type that allows a data-assimilative, eddy-resolving ocean model to accurately map the mesoscale (e.g., Hurlburt, 1984; Hurlburt et al., 2000). Here, this is illustrated in the northern Arabian Sea and the Gulf of Oman by comparing eddies seen in three ocean model nowcasts with eddies seen in a SeaWIFS ocean color image (Fig. 2). Such a cloud-free image during a very large outbreak of high chlorophyll is an unusual event in this region. In the model with atmospheric forcing but without assimilation of the SSH and SST data, the position of the eddies is poorly represented. This is expected because these features are largely non-deterministic due to flow instabilities. With the assimilation, the positions of eddies at both 1/16° and 1/32° resolution are in good agreement with the advective effects in the SeaWiFS imagery, e.g. note the column of 4 alternating counterclockwise and clockwise eddies extending southward from the coast of Iran. These eddies were depicted by assimilating GFO, ERS-2 and Jason-1 altimeter data into the 1/32° ocean model but only data from GFO and ERS-2 in the operational 1/16° model, since Jason-1 data were not yet available in real-time at NAVOCEANO. By using the finer resolution model with data from a third altimeter, some of these features and some smaller features are more accurately positioned and shaped, e.g., the eddy centered near 18°N, 62°E and an observed cyclonic eddy in the Gulf of Oman (at approximately 57.5°E, 25°N), which is anti-cyclonic in the 1/16° model.

3.1.1. A quantitative analysis of model eddy center location error

A quantitative analysis of model eddy center location error in comparison to the ocean color is provided in Fig. 3A and Table 1. All but one eddy with a clearly defined center in the ocean color were used. The exception is the cyclonic swirl located inside a large anti-cyclonic eddy (northeast part of #3). The first search for eddies in the ocean color map was done independently of the ocean model results. This search identified 19 eddies

in the ocean color. As a second pass, the 1/32° and 1/16° data-assimilative ocean models were used as an aid in finding more eddies in the ocean color. This search yielded one more eddy, the smallest one (#20). Eddy #20 is about 1/4° in diameter in both the ocean color and the data-assimilative 1/32° model (the only one to capture it). Some eddies, especially anti-cyclonic eddies, do not have a clearly defined center in the ocean color. Only 35% of the eddies identified in the ocean color were anti-cyclonic. Anti-cyclonic eddies generally lack the upwelling and inward spiral commonly associated with cyclonic eddies, although rapidly strengthening anti-cyclonic eddies can have anti-cyclonic inflow (Hurlburt and Thompson, 1976) and sinking. Sinking is a characteristic unfavorable to phytoplankton.

The latitudes and longitudes of the eddy centers in the ocean color were determined first and without any reference to the model results. The eddy centers in the model results were determined primarily from the velocity field, secondarily using the SSH field because the ocean color field is strongly influenced by advection. The model eddy centers were determined as independently as possible from the ocean color and each other. In this process the model and ocean color eddies were compared only to the extent needed to match them up geographically and determine that they had the same sense of rotation and similar diameters. To qualify as a match the model eddies had to meet all three of these criteria. To match geographically the model eddy and the ocean color eddy had to overlap or be capable of overlapping on a week-long time-scale using a differential propagation speed up to 10 km/day. The preceding is based on the assumption that some eddies were depicted by assimilation of altimeter data at least a week in the past. For the smaller eddies, this gives an upper bound on the eddy center location error of ∼ 100 km. However, 55 km is the largest error in Table 1 for any small eddy where this upper bound value applies. The accuracy in determining the locations of the eddy centers is typically 10–15 km for both the ocean color and the models.

The eddies in Table 1 are listed in the order of decreasing diameter as seen in the ocean color. The purpose is to aid in assessing the eddy mapping skill of the ocean models assimilating satellite altimeter SSH as a function of decreasing eddy size. The first four eddies are ∼ 2° or more in diameter, eddies 5–8 ∼ 1°, 12–16 ∼ 1/2° and 17–20 ∼ 1/4°. With a few exceptions, model eddies 12–19 are typically ∼ 1/2° to 3/4° in diameter with the remainder generally about the same as depicted in the ocean color. A 1/4° model eddy like #18 or #20 is 8 grid points in latitude by 6 points in longitude in the 1/32° model, about the smallest it could realistically depict.
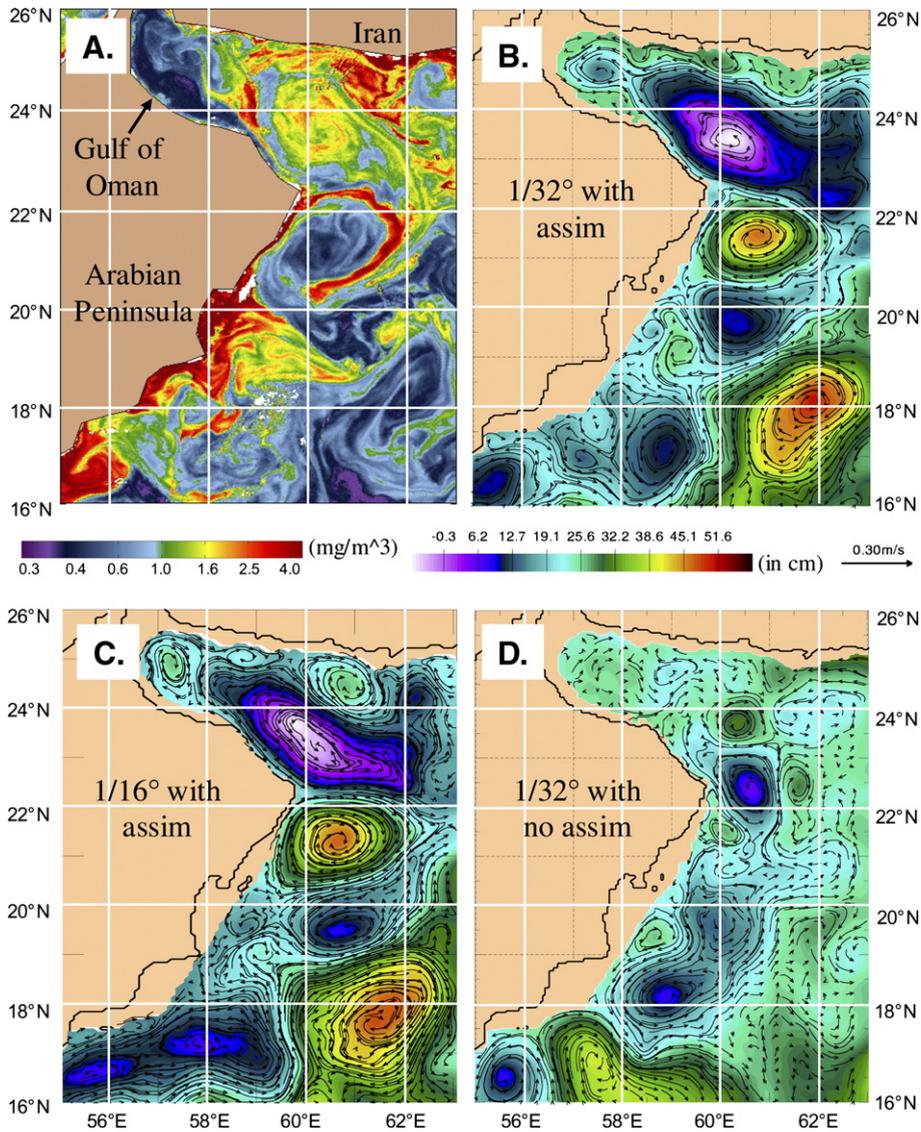
Fig. 2. A comparison of (A) chlorophyll concentration from SeaWiFS (2–6 Oct. 2002 latest cloud free pixel composite with most data from 6 Oct.) with (B–D) NLOM SSH (with surface currents overlain) from 6 Oct. 2002, (B) 1/32° model with SSH and SST assimilation, (C) 1/16° model with the assimilation, and (D) 1/32° model without the assimilation. All were subject to atmospheric forcing. In (D) the positions of most eddies are poorly represented because they are predominantly non-deterministic due to flow instabilities. With the assimilation of SSH data from satellite altimeters, the eddy positions show good agreement with advective effects in SeaWiFS imagery, e.g. note the column of 4 alternating counterclockwise and clockwise eddies extending southward from the Iran coast. In order to facilitate inter-comparison, a constant offset (7 cm) was subtracted from (C) to better reference it to the areal mean in (B) and (D).

The 1/32° NLOM with assimilation of SSH from 3 altimeters was able to depict 90% of the 20 eddies seen in the ocean color, all of the largest 10, 8 of the 10 smallest vs 70% depicted by the 1/16° NLOM with assimilation from 2 altimeters, 8 of the 10 largest and 6 of the 10 smallest. The 1/32° NLOM with no synoptic ocean data assimilation depicted 35% of the eddies, 2 of the 10 largest and 5 of the 10 smallest. The median center location error for the eddies depicted is 29 km for the 1/32° NLOM with assimilation, 35.5 km for the 1/16° NLOM with assimilation and 42 km for the 1/32° NLOM with no assimilation. All 20 of the eddies seen in the ocean color were depicted by at least one of the two data-assimilative models. The 1/32° NLOM with assimilation had the lowest center location error for 57.5% of the eddies, the 1/16° NLOM for 27.5% of the eddies and the 1/32° NLOM with no assimilation for 15% of the eddies.
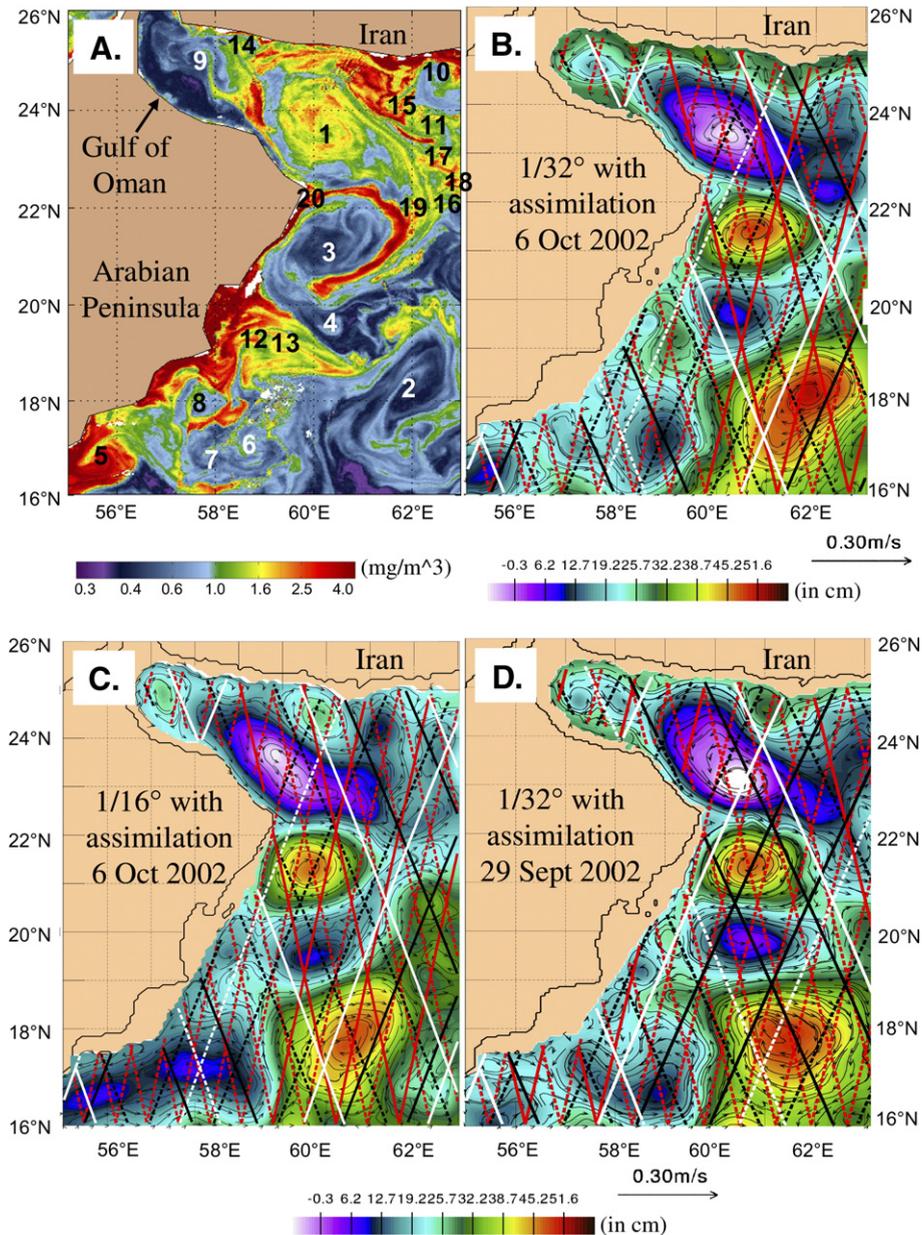
Fig. 3. (A) Same as Fig. 2A with clearly defined eddy centers numbered in order of decreasing eddy size (see Table 1). Number color varies only for visual clarity. (B, C) Same as Fig. 2B, C with the most recent week of observed altimeter tracks overlaid as solid lines and the remaining tracks as dashed lines, red for ERS-2, black for GFO, and white for Jason-1. At that time Jason-1 data were not available in real-time at NAVOCEANO and thus not assimilated by the operational 1/16° NLOM system, but the tracks are overlaid on (C) for reference. (D) Same as (B) but for 1 week earlier.

3.1.2. Effectiveness of altimeter data assimilated by the models in depicting small eddies, 25–75 km in diameter

How effective is the assimilation of satellite altimeter data in depicting the smaller eddies? The 1/32° NLOMn with no assimilation of synoptic ocean data contains numerous small eddies and one might expect that some of these would match up with real eddies seen in the ocean color by chance, because of geometric constraints (e.g. for

eddies near the boundary) and/or because of the atmospheric forcing. The ten smallest eddies shown in the ocean color (11–20) will be used to investigate this issue. Only two are adjacent to a coastal boundary, #14 and #20. Eddy #14 is depicted by all three models in Table 1 and with similar location error, while #20 is only present in 1/32° NLOM with the altimeter data assimilation. This suggests that a boundary indentation in combination with wind

Table 1
Eddy center location errors in ocean prediction models compared to ocean color from SeaWiFS in the northwestern Arabian Sea and Gulf of Oman

Ocean color eddy ID#	A or C	Ocean color eddy center location		1/32° NLOM	1/16° NLOM	1/32° NLOMn no assim
		°N	°E	Eddy center position error in km		
1	C	23.55	60.2	18	35	NP
2	A	18.3	62.0	28	103	NP
3	A	21.15	60.25	58	44	NP
4	C	19.65	60.4	12	43	45
5	C	16.8	55.65	42	35	31
6	C	17.0	58.9	17	42	NP
7	C	16.7	57.9	79	53	NP
8	A	18.0	57.6	40	NP	NP
9	C	25.1	57.6	39	NP	NP
10	A	24.7	62.5	35	30	NP
11	C	23.7	62.3	22	*	42
12	C	19.3	58.8	30	30	NP
13	A	19.225	59.35	11	35	NP
14	A	25.3	58.55	33	36	30
15	C	24.1	61.75	NP	55	47
16	C	22.25	62.7	*	14	*
17	C	23.1	62.55	13	NP	NP
18	A	22.5	62.85	51	18	44
19	C	22.05	62.05	23	NP	26
20	C	22.2	59.95	12	NP	NP

% of eddies present						
90%		70%				35%
Median eddy center position error in km						
29		35.5				42
% of eddies with most accurate position						
57.5%		27.5%				15%

Notes:
The ocean color eddy ID numbers are plotted on Fig. 2a. Eddies are listed in order of decreasing size as depicted by the ocean color. Eddy position measurement error is 10–15 km in both the ocean color and the models.
A, C: A for anti-cyclonic eddies, C for cyclonic eddies.
1/32° NLOM: 1/32° NLOM system with assimilation of altimeter track data from ERS-2, GFO and Jason-1 altimeters.
1/16° NLOM: Operational 1/16° NLOM system with assimilation of real-time altimeter data from the ERS-2 and GFO altimeters (Jason-1 not in the operational data stream at that time).
1/32° NLOMn: 1/32° NLOM with no assimilation of ocean data, only atmospheric forcing.
NP: eddy not present.
*A single "fused" model eddy represents two eddies in the ocean color and the model eddy center lies between the two observed eddies. The model eddy center position error is listed only under the closer ocean color eddy in Table 1. Eddies 16 and 19 are fused in both 1/32° NLOM and 1/32° NLOMn, with eddy center location errors of 23 km (26 km) for eddy #19 and 53 km (54 km) for eddy #16 in 1/32° NLOM (1/32° NLOMn). Eddies 11 and 15 are fused in 1/16° NLOM with eddy center location errors of 55 km for eddy #15 and 60 km for eddy #11. See Section 3.1.4 for discussion of the fused eddies.
Both 1/32° model versions of eddy #18 lie east of 63°E and thus are not depicted in Fig. 2B, D or Fig. 3B.

forcing is sufficient to generate eddy #14. Fig. 3B, D shows that a Jason-1 track (not assimilated by 1/16° NLOM) also influenced the depiction of eddy #14 in 1/32° NLOM, but otherwise eddy #14 is poorly observed by the most recent 3 weeks of satellite altimetry.

Overall, 1/32° NLOM captured 80% of the 10 smallest eddies in Table 1 vs 60% by 1/16° NLOM and 50% by 1/32° NLOMn without the assimilation, and 1/32° NLOM had the lowest eddy center position error for 55% of these eddies vs 25% for 1/16° NLOM and 20% for 1/32° NLOMn. Further, the median position error, for the portion of the 10 smallest eddies depicted, is 22.5 km for the 1/32° NLOM, 32.5 km for the 1/16° NLOM and 42 km for 1/32° NLOMn. Among these eddies, the smallest location error is 11 km for 1/32° NLOM, 14 km for 1/16° NLOM and 26 km for 1/32° NLOMn. Five of the eight small eddies depicted by 1/32° NLOM and two of the six in 1/16° NLOM have location errors <26 km and 87.5% of the small eddies in 1/32° NLOM and 83% of those in 1/16° NLOM have lower eddy center position error than the 1/32° NLOMn median of 42 km.

3.1.3. Source of improvement: model resolution or number of altimeters?

The preceding comparisons between the data-assimilative and non-assimilative models clearly demonstrate the effectiveness of altimeter SSH assimilation in mapping ocean eddies, including the smaller eddies. In addition, the 1/32° NLOM with the assimilation clearly outperforms the 1/16° NLOM with assimilation. However, without additional analysis it is not clear whether this is due primarily to the increased model resolution or to the increase from 2 to 3 altimeters used for SSH assimilation. We do know that the 1/32° model can depict eddies with diameters > 1/4° vs > 1/2° for the 1/16° model. All four of the "1/4°" eddies (17–20) are depicted in the 1/32° model (three with accurate eddy center locations), while the 1/16° model captures only one of these eddies (by depicting it as an eddy > 1/2° in diameter).

This issue is investigated further using Fig. 3B, C, D with the altimeter tracks from all 3 altimeters overlaid on the 1/32° and 1/16° data assimilative results. The Jason-1 altimeter tracks (in white) are included for reference even though the 1/16° model did not assimilate them (Fig. 3C). In all, 6 plots like Fig. 3B–D were examined, 22 Sept., 29 Sept. and 6 Oct. from the data-assimilative 1/16° and 1/32° NLOM. Each had the most recent week of altimeter tracks overlaid as solid lines (the rest as dashed lines). In total, these cover the most recent 3 weeks of altimeter data (16 Sept.–6 Oct.). Although a week of altimeter tracks were overlain as solid lines on each plot, the analyses were performed daily using a 3-

day data window. The length of time used for examining earlier results is based on the model time-scale for forecast skill in this region, as shown in Section 3.5. The influence of the earlier results on the results and comparisons for 6 Oct. were clearly evident.

Examination of the plots indicated that for 80% of the 20 eddies, the existence, location and amplitude in the models were not noticeably influenced by this particular configuration of observed Jason-1 tracks. Eddies 9 and 14 were clearly influenced and eddies 6 and 8 may have been influenced. Despite the Jason-1 influence on eddy #14 in 1/32° NLOM, the results were not improved, as discussed earlier and shown in Table 1. In the case of eddy #9, a recent Jason-1 track crossed the interior of the cyclonic eddy depicted by the 1/32° NLOM on 6 Oct. (Fig. 3B), a location where the model shows a SSH ridge between two cyclonic eddies on 29 Sept. (Fig. 3D). In contrast, an anti-cyclonic eddy was present in 1/16° NLOM, which did not assimilate the Jason-1 data (Fig. 3C). Because the 29 Sept. cyclonic eddy east of the SSH ridge in 1/32° NLOM was propagating westward, it is quite likely it would have merged with the eddy west of the ridge even without assimilation of the Jason-1 track. However, that track would have clearly benefited 1/16° NLOM. This raises the issue of dynamical interpolation skill and the impact of the data assimilation earlier in time. At the beginning of the time frame examined (2 weeks before 6 Oct), the 1/32° NLOM had already pre-conditioned itself with cyclonic eddies in the Gulf of Oman, while the 1/16° NLOM was already pre-conditioned with anti-cyclonic eddies. The 1/32° NLOM without the data assimilation shows only very weak features in the Gulf of Oman (Fig. 2D).

The preceding results strongly indicate that the increase in model resolution had a larger positive impact on the results than the addition of the Jason-1 tracks in this particular situation. In general, earlier studies have found that adding a third nadir beam altimeter modestly reduces the RMS SSH analysis error (Le Traon and Dibarboure, 1999; Hurlburt et al., 2000; Le Traon et al., 2001; Smedstad et al., 2003). Outside of Section 3.1, SSH from the same number of altimeters was assimilated by 1/16° and 1/32° NLOM in most of the tests and all of the comparisons of real-time results. In Section 3.4, the Hawaiian Islands region is used to compare results where both models assimilated data from one or three altimeters.

3.1.4. The roles of altimeter data assimilation and ocean model dynamical interpolation/forecast skill in nowcasting small eddies at 1/16° and 1/32° resolution

Three noteworthy examples illustrate the importance of ocean model dynamical interpolation/forecast skill

and the value of increased model resolution in nowcasting small eddies. The pair of counter-rotating eddies, #12 and #13, provide an excellent example. Also note the current that enters the region near 60°E and ultimately wraps around eddy #12. It is marked by a ribbon of blue in the ocean color and flows northward along ∼ 60°E, then westward north of 18°N and then northward along ∼ 58.5°E until it wraps around eddy #12. The two eddies and the current are seen in both the 1/16° and 1/32° NLOM with assimilation and they are depicted with similar accuracy in comparison to the ocean color, except that the center location of eddy #13 is more accurate in 1/32° NLOM. Neither of the two eddies nor the current is seen in 1/32° NLOMn with no assimilation. However, it is evident in Fig. 3B, C that eddies #12 and #13 were unobserved by the most recent week of altimeter data and only the southernmost portion of the current was observed. Hence, we must explore earlier in time to investigate the role of the altimeter data in forming these observed features and the dynamical interpolation and forecast skill of the models in creating a realistic depiction on 6 Oct.

To start, we note that within the pictured region, the length of the current feeding into eddy #12 is ∼ 600 km. Two and one half weeks would be required for a 40 cm s^{-1} current, comparable to the modelled current speed, to advect the low chlorophyll water that distance, implying that at least the southern part of the current has been a persistent feature for at least that long. Going back 1 week (altimeter data between 1 and 2 weeks prior to 6 Oct. overlaid), we see that the current was better observed but the two eddies were only peripherally observed (Fig. 3D). The current and eddy #12 were already in place. Eddy #13 was just forming in 1/32° NLOM but was already in place in 1/16° NLOM (not shown). Going back 2 weeks (altimeter data 2 to 3 weeks prior to 6 Oct. overlaid) (not shown), we find the genesis of eddy #13 as a WNW bulge from eddy #2. This bulge is well observed by 2 ERS-2 and a GFO track and peripherally by a Jason-1 track. Eddy #13 is not yet present in 1/32° NLOM and is just forming in 1/16° NLOM. Thus, altimeter data 2−3 weeks prior was crucial to the depiction of eddy #13 on 6 Oct, possibly with some assistance in the eddy pinch off from a GFO track a week later (Fig. 3D). Eddy #12 was already present on 22 Sept, but only peripherally observed. Thus, this eddy persisted for at least 2 weeks with little change and was only peripherally observed by 3 weeks of altimeter data, but still it is realistically represented in 1/16° and 1/32° NLOM (but not in 1/32° NLOMn with no assimilation). A shifted version of the current was present on 22 Sept. and it was better observed than on 29 Sept. or 6 Oct.

The second example is the cluster of 6 small eddies consisting of #19, 16, 18, 17, 11 and 15 south to north, where #18 is the only anti-cyclonic eddy in this group. The entire cluster spans just over 2°N–S and 1°E–W. All of these eddies are captured by at least one of the two data assimilative systems, 4 by 1/32° NLOM and 3 by 1/16° NLOM, but 1/32° NLOMn with no data assimilation also captured 4 of the eddies (Table 1). However, for the eddies in the cluster, the eddy center location error is less than the smallest location error in 1/32° NLOMn (26 km) for 75% of the 1/32° and 67% of the 1/16° NLOM eddies depicted. This is consistent with the overall results for the 10 smallest eddies presented earlier, which showed value added for altimeter data assimilation in representing small eddies 25–75 km in diameter. By examining the six plots listed earlier, it was evident that the model depictions of all the eddies were influenced by the altimeter data, mainly from ERS-2 and GFO. The cluster was only minimally and peripherally observed by Jason-1.

Starting with the southernmost eddy and progressing northward, eddy #19 was well observed by an ERS-2 track during the week leading up to 22 Sept. The result on 22 Sept. was a small strong eddy in 1/32° NLOM and in 1/16° NLOM a weaker eddy and narrow SSH trough connected to eddy #1. During the next 2 weeks (through 6 Oct), eddy #19 was not observed by the altimetry. It was well maintained by 1/32° NLOM, but the weak eddy and sharp trough in 1/16° NLOM disappeared by 29 Sept. During the week leading up to 29 Sept., the location of nearby eddy #16 on 6 Oct. was well observed at the crossover of ERS-2 and GFO tracks, but no eddy resulted in either model. In 1/32° NLOM there was an ENE extension of the SSH trough associated with eddy #19 which had the ERS-2 track crossing the eastern edge of it just north of the crossover. During the week leading up to 6 Oct, a GFO track crossed the center of eddy #16 and an ERS-2 track crossed the eastern interior. The result was a weak eddy #16 in the 1/16° NLOM (14-km eddy center location error), but only a modification of the existing SSH trough in 1/32° NLOM. In 1/32° NLOM eddies 16 and 19 were fused with the model eddy encompassing both and with the eddy center between them, but much closer to eddy #19 (23-km eddy center location error). Anti-cyclonic eddy #18 just to the north was well observed by altimetry during the weeks leading up to both 29 Sept. and 6 Oct. Both 1/16° and 1/32° NLOM were pre-conditioned to represent this eddy, but 1/16° NLOM was better pre-conditioned and matched the observed eddy center much more accurately.

Northwest of eddy #18 an ERS-2 track passed close to the observed location of eddy #17 on 6 Oct. during the week leading up to 29 Sept. This formed an SSH trough linked to eddy #1 in 1/32° NLOM. During the week leading up to 6 Oct. a GFO track crossed the neck of the trough and also formed an SSH ridge to the south narrowing the trough, both assisting in cutting off eddy #17 and giving an eddy center location error of only 13 km. The 1/16° NLOM did not represent these features with sufficient amplitude and sharpness to form eddy #17, which had an SSH diameter of only 1/2°E–W by 1/4°N–S in 1/32° NLOM, smaller than the 1/2° limit for realistic representation of eddies in 1/16° NLOM.

An ERS-2 and a GFO track passed close to the enter of eddy #15 during the week leading up to 6 Oct, but did not create or pass over an eddy in either model (#15 was not present in 1/32° NLOM). A GFO track crossed the eddy in 1/16° NLOM during the week leading up to 22 Sept. and the eddy propagated westward toward the observed location of eddy #15 on 6 Oct. The 1/32° NLOM was not well pre-conditioned to represent this eddy. Slightly farther to the south (and east of 63°E), the same GFO track crossed the northeastern quadrant (southwestern quadrant) of a larger cyclonic eddy depicted in 1/32° NLOM (1/16° NLOM) on 22 Sept. During the week leading up to 29 Sept., a GFO track crossed the southeastern quadrant of the eddy in 1/32° NLOM, favorably impacting its westward propagation into the observed position of eddy #11 on 6 Oct. (22-km eddy center location error). This occurred during a week when it was not observed by altimetry. The eddy in 1/16° NLOM lay east of the GFO track on 29 Sept. Thus, its propagation did not benefit from the GFO track and eddy #11 was not represented in 1/16° NLOM.

The smallest eddy, #20, provides the third example. It is cyclonic and was not observed by altimetry. It formed where a boundary current associated with anti-cyclonic eddy #3 separated from the boundary. Eddy #3 and the boundary current separation are represented with comparable realism in both 1/16° NLOM and 1/32° NLOM. However, eddy #20 is seen only in 1/32° NLOM. At 1/4° in diameter in both the model and the ocean color, it is smaller than the 1/2° minimum for realistic depiction in 1/16° NLOM. In 1/32° NLOM three such eddies are observed farther south on 22 Sept. (not shown). As eddy #3 moves northward, 1/32° NLOM depicts a cyclonic eddy (#20) in the location observed in the ocean color on 6 Oct. (Fig. 3A) on both 29 Sept. (Fig. 3D) and 6 Oct. (Fig. 3B) (12-km eddy center location error on 6 Oct.). The accurate location of the eddy may be facilitated by a slight boundary indentation not present in the 1/16° NLOM boundary.

The preceding results show that 1/16° and 1/32° NLOM are skilled at using multiple altimeter tracks from

multiple satellites, assimilated through time and space, to build coherent mesoscale features that are consistent with observations, including small eddies. They also demonstrate that 1/32° NLOM has greater skill than 1/16° NLOM, especially for small eddies 25–75 km in diameter. In addition, they show that a model with dynamical interpolation skill can use data assimilation to produce an ambience more conducive to the formation of poorly observed eddies than the same model without the assimilation, a capability that is especially useful in representing small eddies and one that is clearly demonstrated by the results in this subsection.

3.2. Caribbean/Gulf of Mexico

The increase in horizontal resolution produces significant changes in the Caribbean/Gulf of Mexico region (Fig. 4). Transport through 11 of the 14 Caribbean passages is more realistic at the finer resolution, including more realistic Gulf of Mexico inflow through the

Yucatan Channel. The improvement in the Yucatan Channel transport occurs primarily because the flow in the 1/32° model is more surface-trapped than at 1/16°, so more of the transport passes through the Caribbean passages (since more is above the sill depths). In the 1/32° model there is less transport through the Northwest Providence Channel (feeds into the western boundary current near 26°N) in better agreement with observations. Unlike the 1/16° model, the narrowest point in the Florida Strait (along 80°W extending back to the Gulf of Mexico outflow) is north of this channel, as observed.

The improvement in Yucatan Channel transport is particularly significant because it feeds the Loop Current which sheds large eddies in the Gulf of Mexico. The value added of the finer resolution in the Gulf of Mexico is illustrated in a comparison of SeaWiFS ocean color with SSH from the 1/16° and 1/32° models (Fig. 5). Both assimilate SSH data from the GFO and Jason-1 altimeters plus SST. The key features are the Loop Current and a shed eddy. The SeaWiFS imagery shows these as
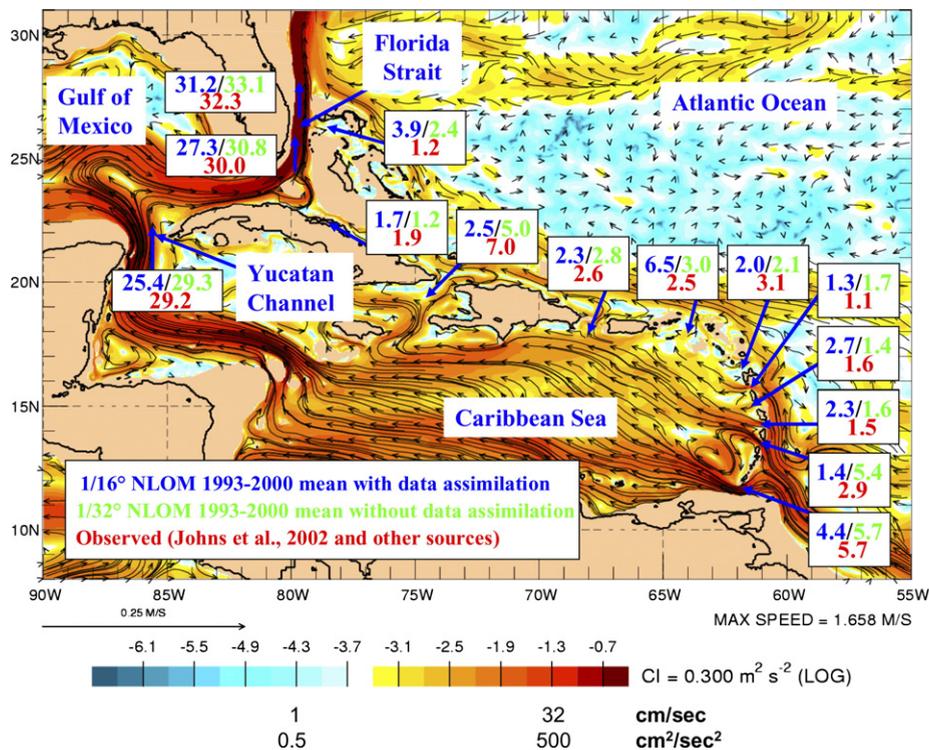

Fig. 4. Observed transports in Sv (10^6 m^3 s^{-1}) vs model mean (1993–2000) transports through Intra-Americas Sea passages at resolutions of 1/16° (with data assimilation) and 1/32° (without data assimilation), the most suitable estimates we had from each model over an extended common time period. There are no data-assimilative 1/32° model results prior to Oct. 2000 and the passage transports are not strongly constrained by the data assimilation. Also shown are 6-year mean currents from the 1/32° model (climatological forcing only) superimposed on their strength. Johns et al. (2002) provided the best estimates based on observations and did not adjust them to provide a closed mass budget. The "observed" value of 29.2 Sv for the Yucatan Channel used here was obtained by subtracting the two observed Florida Strait inflows between Yucatan and 27°N (1.2 and 1.9 Sv) from the well determined value of 32.3 Sv at 27°N given by Larsen (1992). The sum from the remaining Caribbean passages gives a second observationally based estimate of 28.0 Sv for Yucatan Channel. [Figure courtesy T.L. Townsend, Naval Research Laboratory].
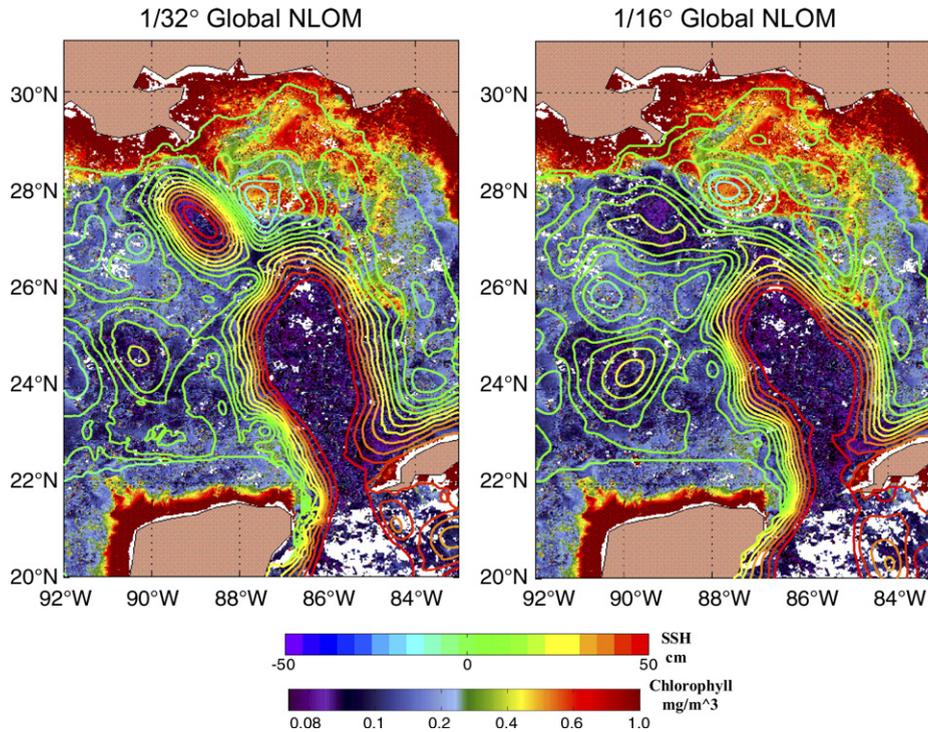
Fig. 5. A comparison of SeaWiFS ocean color with SSH from the 1/32° and 1/16° data assimilative systems. Model SSH from 28 Aug. 2003 overlain on SeaWiFS chlorophyll concentration from 22 to 28 Aug. 2003 latest cloud free pixel composite. SSH data from the GFO and Jason-1 altimeters were assimilated. SSH contours > 50 cm are omitted.

dark areas of low chlorophyll outlined by a Mississippi River plume of high chlorophyll (red and yellow) along the eastern edge of the eddy and the Loop Current. The 1/16° model largely misses the shed eddy. In an animation covering June–Sept. 2003, the 1/32° NLOM routinely outperformed the 1/16° model. In a more detailed comparison of 5 data-assimilative ocean prediction systems covering the Gulf of Mexico, Chassignet et al. (2005) found that the 1/32° NLOM system performed the best in comparison to ocean color imagery with a 1/12° Atlantic HYCOM system a close second. Animations comparing these five systems can be found on the NLOM and HYCOM web pages (http://www.ocean.nrlssc.navy.mil/global_nlom and http://www.hycom.org). Besides the improved inflow through Yucatan Channel, other reasons for better performance at 1/32° resolution are better dynamical interpolation of the assimilated altimeter data and elimination of a southward leakage of the Deep Western Boundary Current through the Florida Straits (found in the 1/16° model) via a modification to the bottom boundary condition. The southward leakage in the 1/16° model resulted in a westward subthermocline current along the continental slope in the northern Gulf of Mexico. Such a current can advect upper ocean currents (Hurlburt and Thompson,

1980; Hurlburt et al., 1996) (e.g. the semi-detached Loop Current eddy in Fig. 5), and in this case damage the dynamical interpolation skill of the 1/16° model in the northern Gulf of Mexico, as illustrated in the figure.

3.3. Gulf Stream

Fig. 6 shows results from the climatologically-forced 1/32° global model in the Gulf Stream region, one of the most challenging regions to simulate in the world ocean. It also shows comparisons to the corresponding 1/16° climatological global simulation and to observations. The mean SSH from each model is overlain by the 15-year mean north wall of the Gulf Stream from satellite IR (middle line) flanked by lines one standard deviation away. The RMS SSH variability is compared with the Gulf Stream mean axis (center) flanked by the standard deviation about the mean axis and extreme positions determined from Topex/Poseidon data (Lee, 1997). Both models show a realistic mean Gulf Stream pathway, although the 1/16° model has a slight northward bulge near 70°W. Resolution of 1/16° or ~ 7 km is the minimum required to obtain a realistic Gulf Stream pathway (Hurlburt and Hogan, 2000). At coarser resolution, the pathway is very unrealistic and the Gulf Stream transport
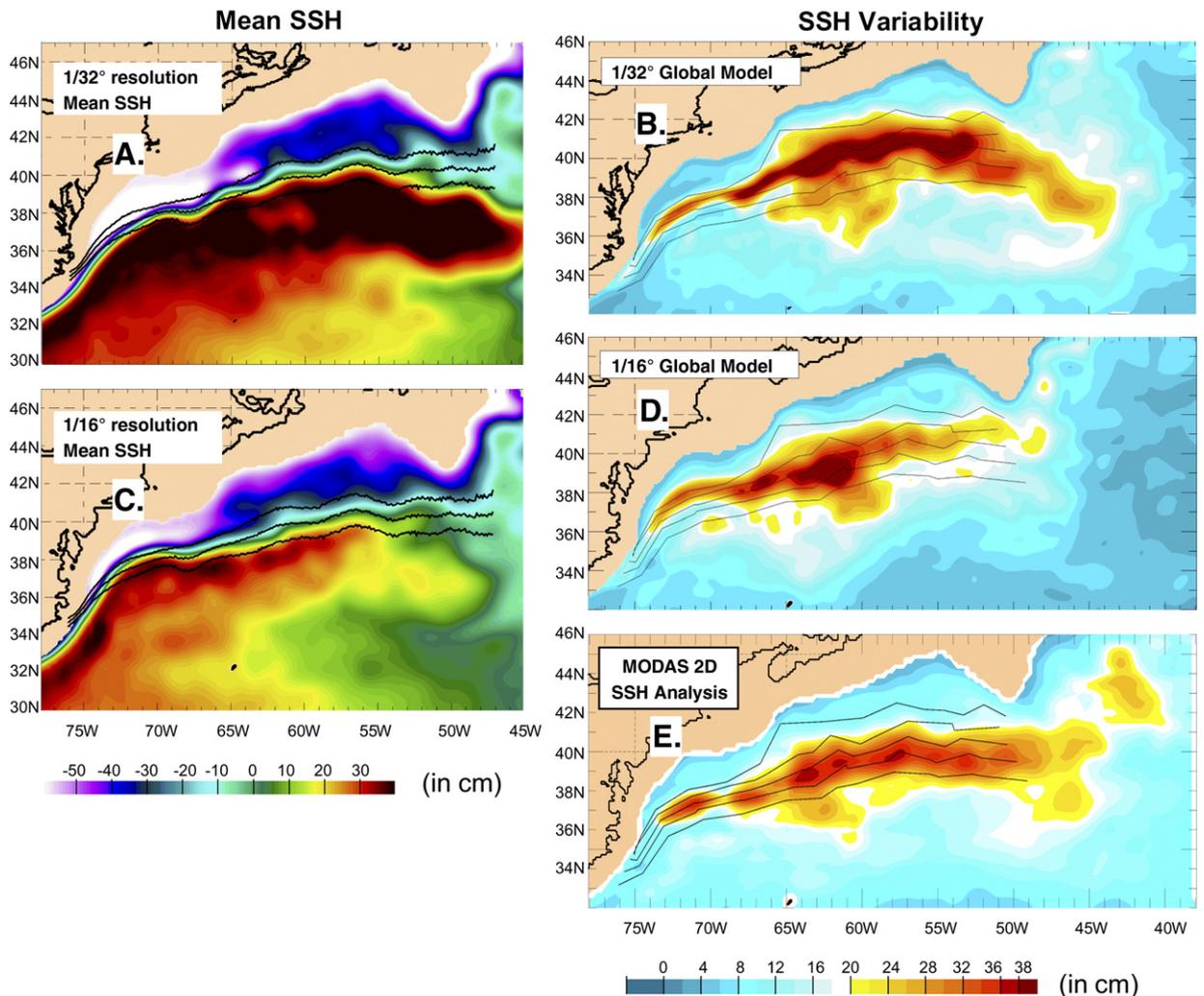
Fig. 6. Mean SSH (A, C) and RMS SSH variability (B, D) in the Gulf Stream region from the 1/16° and 1/32° global NLOM with climatological forcing and no assimilation of SST or SSH data. Panel E depicts RMS SSH variability (1993–2003) computed from the model independent MODAS 2D daily altimetric SSH analyses. The lines overlain in A and C depict the mean pathway of the Gulf Stream IR north wall 1982–1996±1 standard deviation by Cornillon and Sirkes (unpublished work). The 5 lines overlain in B, D and E are the Gulf Stream mean axis (center), standard deviation about the mean axis and extreme positions determined from Topex/Poseidon data (Lee, 1997). The Gulf Stream (depicted by the tightly packed contours) robustly separates from the coast near Cape Hatteras (approximately 36°N, 75°W) and follows a realistic pathway to a region south of the Grand Banks (approximately 42°N, 50°W).

is much too weak. However, a realistic pathway is more easily and robustly obtained at 1/32° resolution and the Gulf Stream transport is much higher and more realistic, particularly south of the Grand Banks at 50°W between 36 and 44°N (77 Sv at 1/32° and 42 Sv at 1/16° for the baroclinic transport vs an estimate of 65 Sv in the upper 1000 m by Dietrich et al. (1980)). Associated with this large increase in transport is a large increase in the strength and eastward penetration of the non-linear recirculation gyre on the south side of the Gulf Stream (shown in red and black). This alters the large-scale C-shape of the subtropical gyre.

The RMS SSH variability is more realistically distributed in the 1/32° model, with higher variability protruding farther to the east, consistent with RMS SSH (1993–2003) computed from the model-independent MODAS2D SSH analyses that are operational at NAVOCEANO (Fox et al., 2002). Further, the pattern and amplitude of the variability are helpful in assessing the ability of the climatologically-forced model (without data assimilation) to simulate specific features of the mean flow and variability. Both the 1/16° and 1/32° models show the narrow corridor of Gulf Stream variability west of ~ 69°W with low variability to the north of this corridor.

However, the corridor bulges too far north in the 1/16° model. Both models also simulate the southward extension of high variability near the New England Seamount Chain (~ 60°–65°W), a region of high cold core ring generation with a westward trail of elevated variability as the rings propagate to the west, features better represented in the 1/32° model. The largest advantage of the 1/32° model is demonstrated by using the pattern of high variability to assess the eastward penetration of the non-linear recirculation gyre and its latitudinal position in that region. Both the 1/32° model and MODAS2D variability show eastward penetration to ~ 44°W near 37°–38°N and a wraparound pattern of high variability to the southern edge of the gyre along 35°–36°N. However, even the 1/32° model fails to reproduce the northeastward extension of high variability (41°–45°N, 40°–45°W) associated with the Mann Eddy east of the Grand Banks. See Hurlburt and Hogan (2000) for additional discussion of other NLOM simulations vs observed SSH variability in the Gulf Stream region.

The improvements in the simulation of the Gulf Stream at 1/32° resolution have nowcast/forecast implications, as is illustrated in Fig. 7. The Gulf Stream in the data assimilative 1/32° model is more realistic, following the meanders indicated in the operational IR frontal analyses performed at NAVOCEANO better than at 1/16°. In addition, the Gulf Stream is stronger and more inertial in the 1/32° model as indicated by the larger change in SSH across the stream. The improvements in the nowcast Gulf Stream pathway provide a better forecast initial condition, and hence a more accurate forecast as well. This is seen in axis error statistics shown in Fig. 8. The error is calculated as the area between corresponding SSH contours in the forecast and the
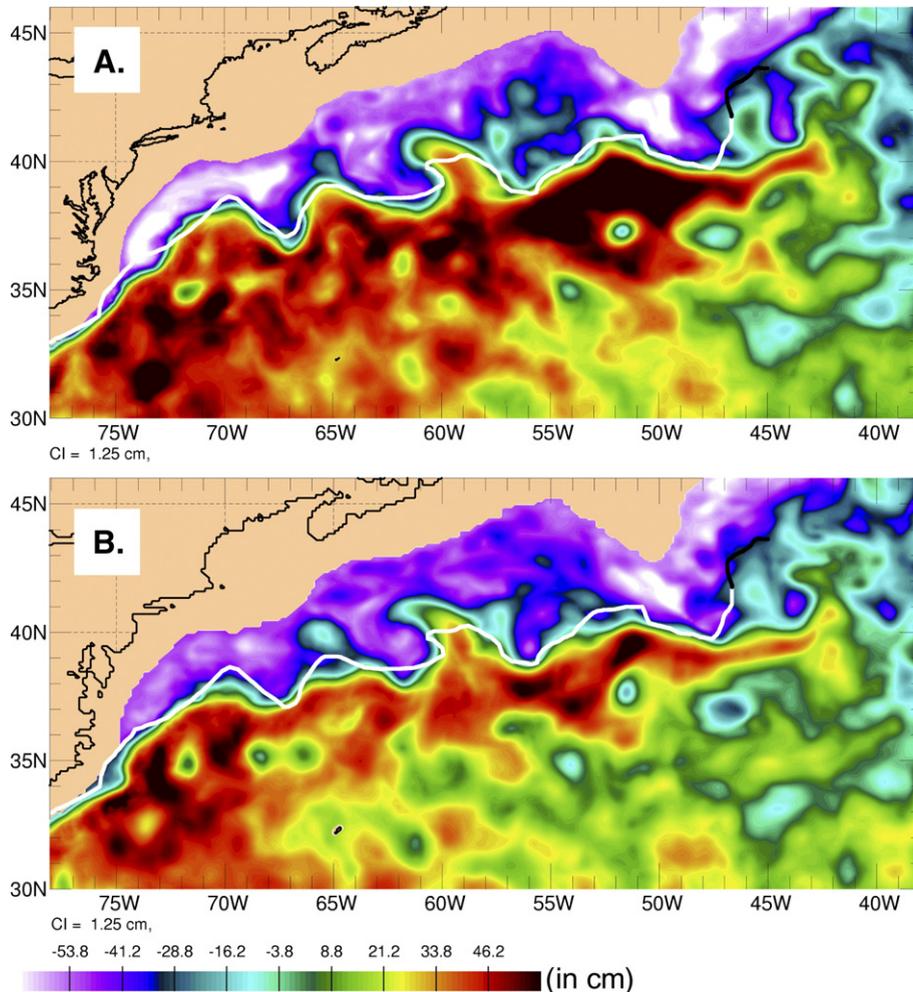

Fig. 7. Nowcast SSH in the Gulf Stream region from the (A) 1/32° and (B) 1/16° global NLOM systems for 12 May 2003. The lines overlain are operational IR frontal analyses by the Naval Oceanographic Office; black lines are segments based on IR data > 4 days old.
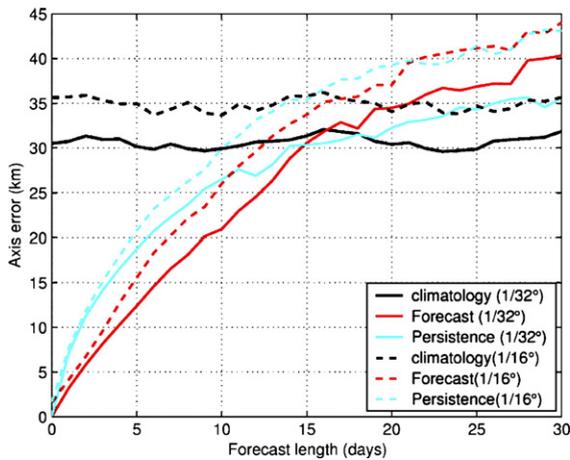
Fig. 8. Mean axis error for 24 Gulf Stream forecasts from the 1/16° (dashed lines) and 1/32° (solid lines) nowcast/forecast systems initialized during the time period 1 June 2001–31 May 2002. The forecasts from the 1/32° model have lower axis error for the duration of the forecast.

verifying analysis divided by the contour length in the analysis. Since we are using the model analysis as the "truth", we use several different SSH contours to represent the Gulf Stream pathway and calculate an average error for these contours. Throughout the forecast period, the 1/32° system exhibits lower error for the Gulf Stream axis.

3.4. Hawaii

The ability of satellite altimetry to constrain an eddy-resolving model was discussed in Section 3.1. Where the mesoscale variability is highly non-deterministic, as in the region around the Hawaiian Islands, insufficient data to constrain the model can introduce significant errors into the nowcast. Hurlburt et al. (2000) and Smedstad et al. (2003) discuss the suppression of nowcast SSH error as the number of altimeters used in assimilation is increased. Fig. 9 (A) and (B) shows a comparison of 1/16° and 1/32° NLOM SSH snapshots for 19 March 2004 in the Hawaii region when data from only 1 satellite altimeter (Jason-1) were assimilated. The snapshots show some qualitative similarities, but large differences can also be noted (e.g., robust eddies in the 1/32° SSH nowcast at approximately 157°W/18.5°N, 157°W/19.8°N and 156°W/22°N that the 1/16° model doesn't exhibit). This occurs because data from 1 altimeter are not sufficient to adequately constrain the models in this region and thus they are unable to skillfully map the mesoscale eddies, which are predominantly non-deterministic in relation to atmospheric forcing.

Fig. 9 (C) and (D) show a comparison of SSH snapshots from the 1/32° and 1/16° models on 5 June 2004 when data from 3 satellites (Jason-1, GFO and Envisat) were assimilated. The solutions show better agreement with an anomaly correlation of .94 for the SSH in panels (C) and (D) vs .30 for panels (A) and (B). In addition, animations of this area from the 1/32° model tend to show better time continuity of small-scale features. In the Hawaii region we see much larger impacts from the resolution increase and the data increase from one to three altimeters than in the northern Arabian Sea (Figs. 2, 3, Table 1). In that case the resolution increase and an increase from 2 to 3 altimeters gave clear improvement, but less dramatic than here.

The finer resolution model also gives improvement in comparison to SSH from four tide gauges in the Hawaiian Islands (30-day moving average applied, not shown) with reduced RMS error at all four and an overall 19% reduction in the error variance during the 1-year period (June, 2001–May, 2002) used for comparison and statistical evaluation of the two systems. During this period data from 3 altimeters (ERS-2, GFO and Topex/Poseidon) were consistently available. It is noteworthy that while the error variance was reduced by 19%, the SSH variance at all 4 tide gauge locations (over the same time period) increased in comparison to the 1/16° model, overall by 2.2× when the 1/32° model was used to assimilate the data. This improves agreement with the tide gauge variance, i.e. the variance is 4.3 cm^2 for the 1/16° model, 9.7 cm^2 for the 1/32° model, and 15 cm^2 for the tide gauge data.

3.5. Evaluation of nowcast/forecast skill

3.5.1. Model-data comparisons using moored buoys and tide gauges

As in Smedstad et al. (2003), modeled SSH is compared with observations using daily time series from 94 tide gauge stations. A 30-day running mean was applied to filter time-scales not well observed by altimetry. Fig. 10 shows a histogram of RMS difference and correlation statistics between model nowcasts and observed sea level from each model. It is important to note that NLOM assimilates SSH from real-time satellite altimetry, not tide gauges. Both models have comparable RMS difference and correlation statistics (median RMSD ≈ 4.0 cm and median correlation ≈ .80). The distribution of correlations is nearly identical, but the distribution of RMSD shows improvement, with shifting of the distribution to lower RMSD values.

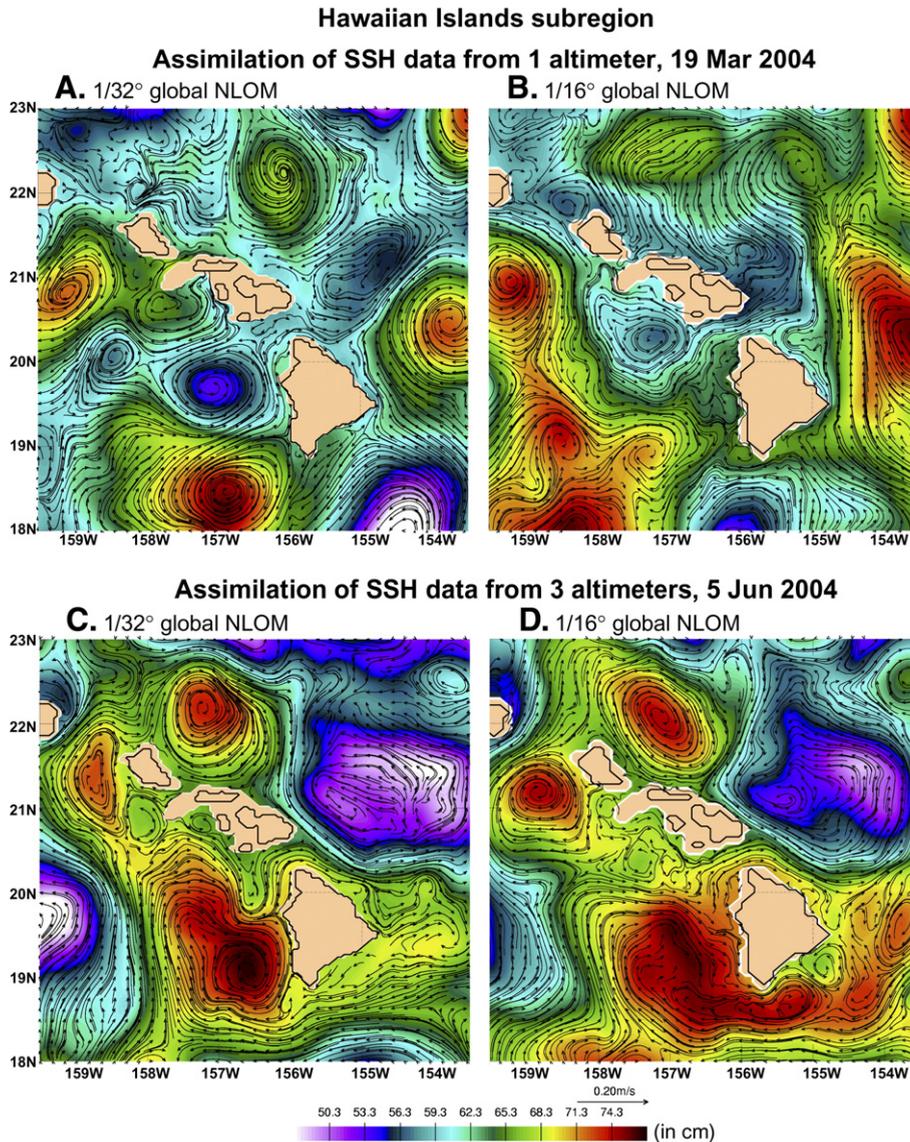Fig. 11 shows a histogram of RMS difference and correlation statistics between daily time series of

Fig. 9. Snapshots of SSH (with surface currents overlain) in the Hawaiian Islands subregion for 19 Mar. 2004 (A and B) and 5 Jun. 2004 (C and D) from the 1/32° (A, C) and 1/16° (B, D) global models (both with assimilation). For 19 Mar. 2004, data from only one satellite altimeter (Jason-1) were assimilated. For 5 Jun. 2004, data from 3 satellite altimeters (Jason-1, GFO and Envisat) were assimilated. To facilitate inter-comparison, a constant offset (4 cm) was subtracted from (B) and (D) to better reference them to the areal mean in (A) and (C).

observed SST and nowcast SST from the 1/32° and 1/16° models. A total of 84 buoys (from the National Data Buoy Center (NDBC) and the TAO and PIRATA arrays) were used in this comparison. NLOM assimilates the MODAS daily operational SST analyses of satellite MCSST data (Sections 2.2 and 2.5). Both models have comparable RMS difference and correlation statistics (median RMSD ≈ .35°C and median correlation ≈ .94). This negligible difference is due to the strong SST assimilation used in both models and lower sensitivity to horizontal resolution than SSH.

3.5.2. Forecast skill

Several metrics are used routinely to assess model forecast skill, all based on comparison to a verifying analysis, and forecast skill superior to persistence (a forecast of no change), and either climatology or some minimum value of the metric. The metrics are RMS error, anomaly correlation, skill score, and for the Kuroshio and the Gulf Stream, axis error (Fig. 8). See Smedstad et al. (2003) for discussion and examples of results from each one. See the real-time NLOM web page http://www.ocean.nrlssc.navy.mil/global_nlom for
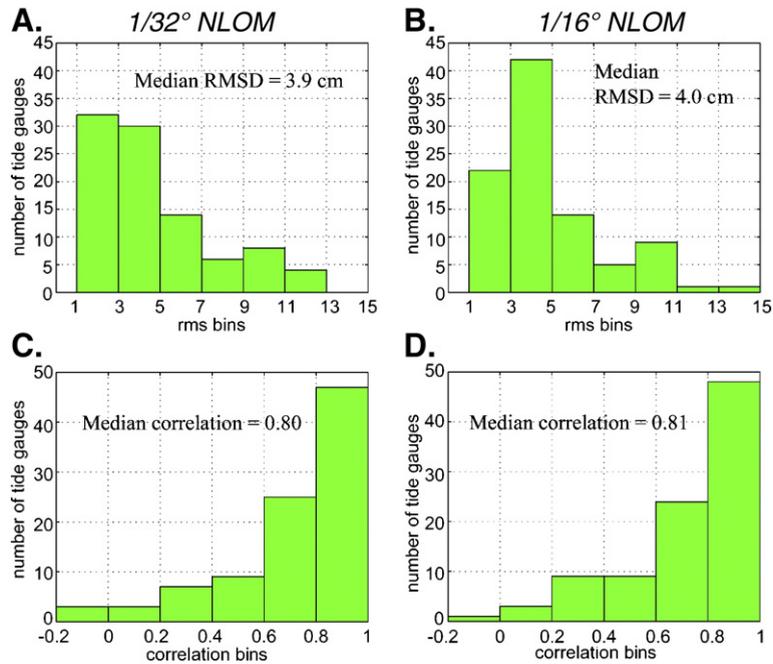
Fig. 10. Histogram of RMS difference (A and B) and correlation statistics (C and D) between observed and model nowcast sea level from the 1/16° and 1/32° NLOM nowcast/forecast systems during the period 1 June 2001–31 May 2002. Note that NLOM assimilates SSH from real-time satellite altimetry, not tides gauges. These comparisons are based on deviations from the mean of each time series. 94 tide gauge stations were used.
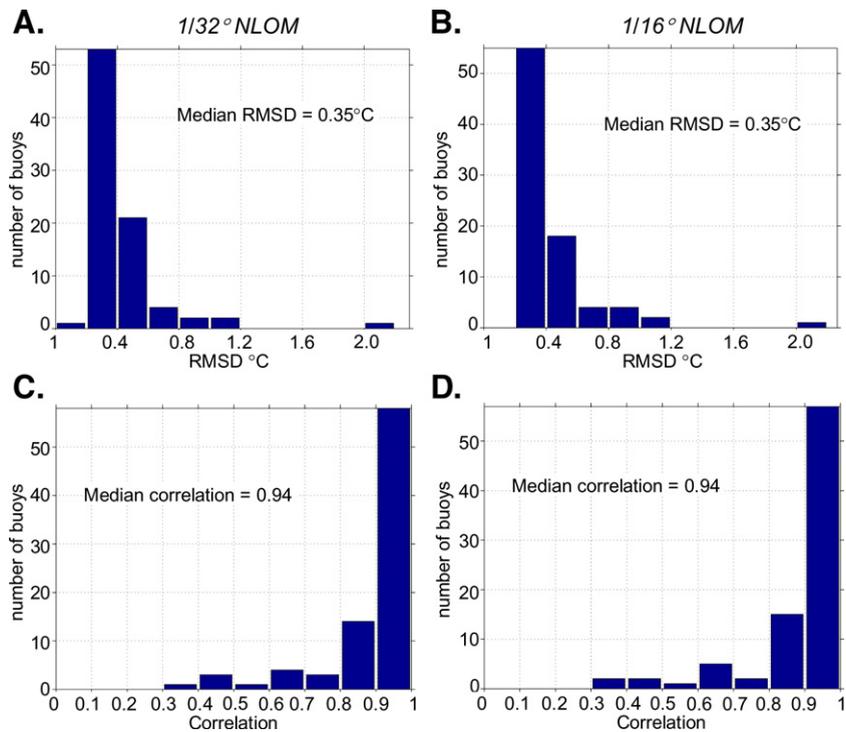

Fig. 11. Histogram of RMS difference (A and B) and correlation statistics (C and D) between observed SST from 84 moored buoys and nowcast SST from the 1/16° and 1/32° NLOM nowcast/forecast systems during the period 1 June 2001–31 May 2002. Note that NLOM assimilates SST from daily operational MODAS SST analyses of satellite MCSST data, which do not include data from moored buoys.

real-time, archived and summary results for each metric in many regions from both the 1/16° and 1//32° models.

Here we focus on one metric, anomaly correlation (AC) between the forecast and the verifying analysis, as is typically done in meteorology. The formula used is identical to that used in Smedstad et al. (2003):

$$AC(f,x) = \frac{\sum (f - \bar{f})(x - \bar{x})}{\sqrt{\sum (f - \bar{f})^2} \sqrt{\sum (x - \bar{x})^2}}$$

where $\bar{f}$ is the model mean and $\bar{x}$ is the mean of the analysis. In this case, the SSH mean of the model and

the analysis is the model mean over 1997 to 2002 with the modifications described in Section 2.3.

Fig. 12 shows AC for the world ocean and 11 subregions averaged over 22 30-day forecasts from the 1/16° and 1/32° models. The higher resolution model has more larger amplitude small-scale features which can get out of phase on shorter time-scales. Therefore, persistence has less skill in the 1/32° system compared to the results at 1/16° resolution. Thus, the best way to judge performance is not by the anomaly correlation for the forecast, but by the spread between the forecast and persistence. In all cases the spread is larger for the 1/32° model on any day where the difference is readily discernable in Fig. 12.
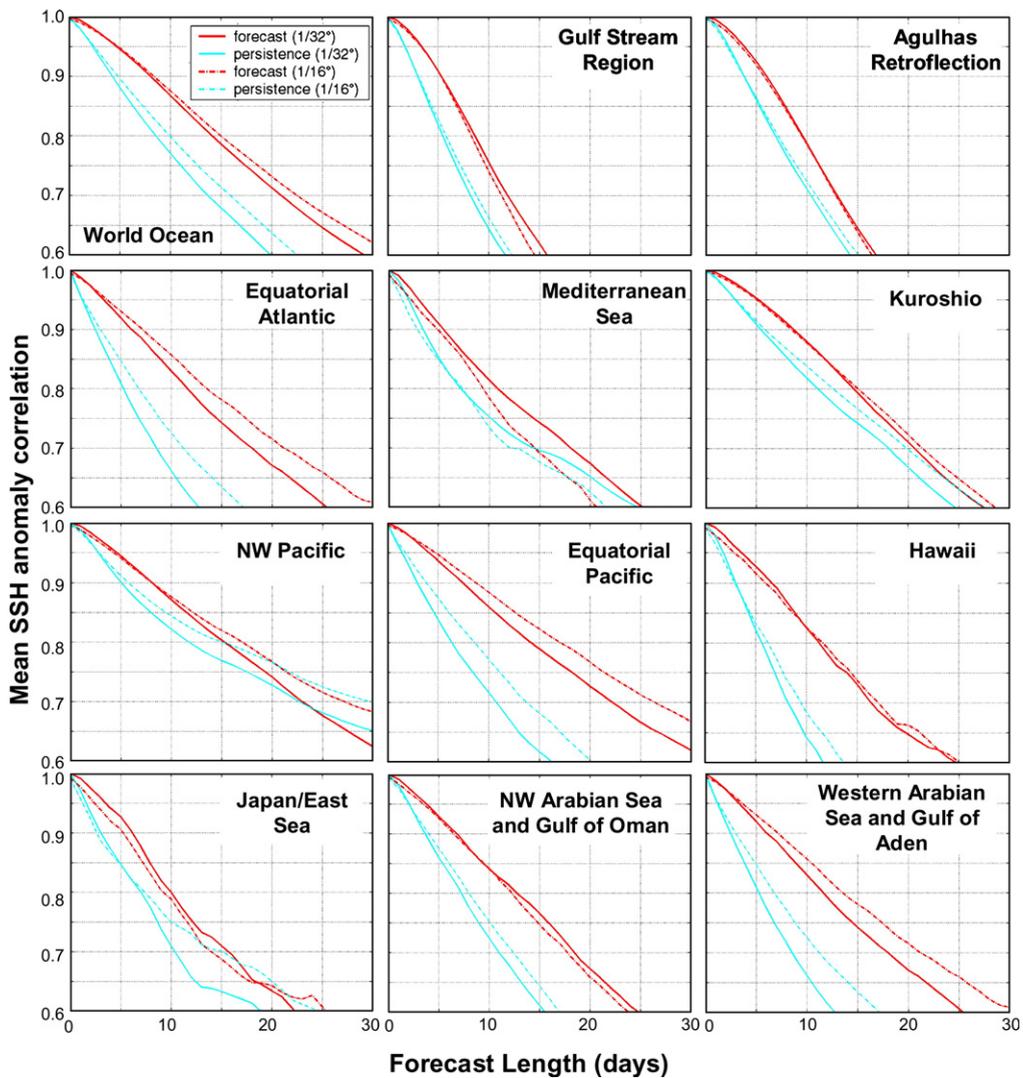

Fig. 12. 1/16° (dashed lines) and 1/32° (solid lines) SSH forecast verification for the global domain and 11 subregions. The verification statistic is anomaly correlation between the model forecast (red) or persistence (blue) and the verifying analysis. The plots show the mean statistics over 22 30-day forecasts initialized during the period 1 June 2001–31 May 2002. See Table 2 for regional boundaries.

Table 2
Regional boundaries of the subregions depicted in Figs. 12 and 14

Subregion name	Latitude range	Longitude range
Gulf Stream region	35°N–45°N	76°W–40°W
Agulhas retroflection	45°S–25°S	0°–50°E
Equatorial Atlantic	20°S–20°N	55°W–15°E
Mediterranean Sea	30°N–47°N	6°W–36°E
Kuroshio	25°N–50°N	127°E–180°
NW Pacific	40°N–58°N	150°E–180°
Equatorial Pacific	20°S–20°N	109°E–77°W
Hawaii	18°N–23°N	159.5°W–153.5°W
Japan/East Sea	34°N–48°N	127°E–142.5°E
NW Arabian Sea and Gulf of Oman	15°N–26°N	51°E–65°E
Western Arabian Sea and Gulf of Aden	EQ–20°N	40°E–60°E

To further compare the forecast skill of the 1/16° and 1/32° systems, 23 30-day forecasts of SSH from each model (initialized during the period 1 June 01–31 May 02) were compared with tide gauge time series at 78 locations (Fig. 13). Tide gauge SSH is not assimilated by either system. A 13-day moving average was applied to filter time-scales not resolved by the assimilated altimeter data. The forecast SSH from the 1/32° system generally agrees better with the tide gauge observations for the forecast duration at both open ocean (island) and coastal tide gauge locations.

3.5.3. Sensitivity of ocean forecast skill to the forcing fields

A significant question, addressed in Smedstad et al. (2003), is the sensitivity of ocean model forecast skill to the use of climatological atmospheric forcing fields beyond the end of the forecast available from an atmospheric model. This question is revisited here in Fig. 14. These results indicate that globally and in many regions of the world ocean the 30-day SSH forecasts are not very sensitive to the difference between the climatological and analysis quality forcing fields. The evolution is more sensitive to the initial state than to the atmospheric forcing anomalies on the time-scale of the 30-day forecasts.

Hurlburt (1984) discusses classes of oceanic response to atmospheric forcing and the corresponding implications for the time-scale of forecast skill. For example, the evolution of mesoscale variability, predominantly due to flow instabilities, typically has low sensitivity to atmospheric forcing on 30-day time-scales. Examples are mesoscale eddies and the meandering and eddy shedding of ocean currents and fronts. These are strongest in regions such as the Gulf Stream, Kuroshio and Agulhas retroflection, but are ubiquitous in the world ocean (e.g., see Figs. 2,3 in the northern Arabian Sea and Fig. 9 in the Hawaiian Islands region). In equatorial regions, shelf break wave guides, and in shallow water (the latter mostly excluded in NLOM), the model response to the wind forcing is more deterministic and the SSH forecast skill improves when analysis
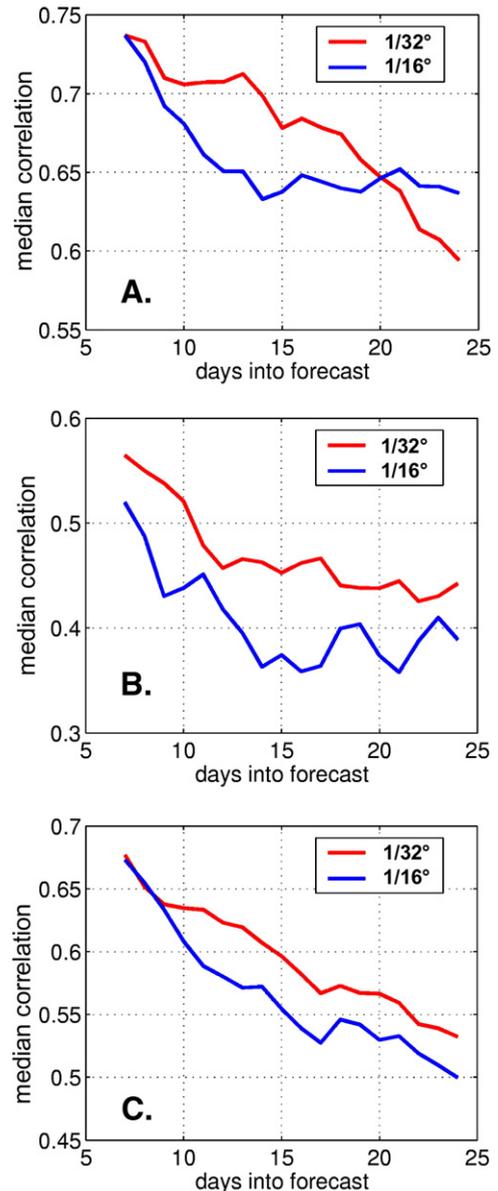

Fig. 13. A comparison of forecast and observed SSH fluctuations from the 1/16° (blue lines) and 1/32° (red lines) NLOM systems. A 13-day moving average was applied to filter time-scales not resolved by the altimeter data. The median correlation statistics (computed over 23 forecasts initialized between 1 June 2001 and 31 May 2002) are computed over (A) tide gauges at open ocean island stations (49 total), (B) coastal tide gauges (29 total) and (C) all tide gauges (78 total). Tide gauge SSH data are not assimilated by the systems.
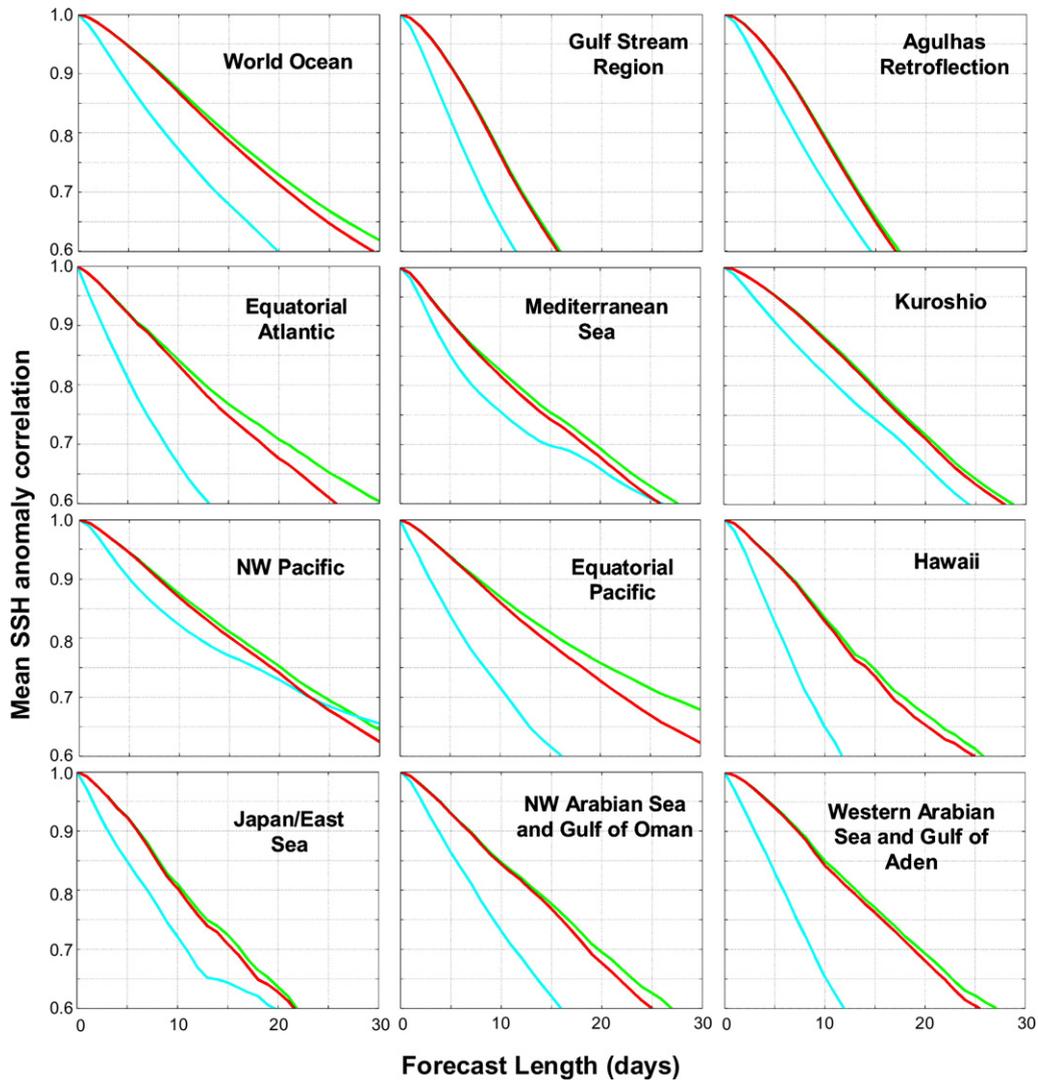
Fig. 14. SSH anomaly correlation of 1/32° NLOM 30-day forecasts with the verifying analysis for the global domain and 11 subregions. The red curve is for the NLOM forecast made with operational forcing; the green curves signify the forecasts which used analysis quality wind and thermal forcing and SST fields, and the cyan curve verifies forecasts of persistence (i.e., no change from the initial state). The results are means for 26 forecasts initialized during the time window 1 June 2001–31 May 2002.

quality winds are used for the duration of the forecast. Even in this case, the propagation of existing equatorial and coastally-trapped waves can be forecast with some skill after the reversion to climatological forcing. Jacobs et al. (1994) even demonstrated ∼ 7-year skill when climatological forcing was used while predicting the propagation of a trans-Pacific Rossby wave (along 30°N) that was generated by the 1982–83 El Niño.

This is a more definitive investigation of the sensitivity of forecast skill to atmospheric forcing than Smedstad et al. (2003), who used 8 forecasts early in 2001 and fewer subregions to address this question. In

this comparison a total of 26 forecasts were used with initial states covering a complete annual cycle from June 2001–May 2002. Also, the quantity and quality of the altimeter data are significantly improved.

4. Summary and conclusions

A 1/32° nearly global ocean nowcast/forecast system has been developed by the Naval Research Laboratory at Stennis Space Center. This system uses the NRL Layered Ocean Model (NLOM) with assimilation of sea surface height from satellite altimeters and sea surface

temperature from multi-channel satellite infrared radiometers. This system has been running in near real-time since 1 Nov. 2003 and daily in real-time since 1 Mar. 2005. It became an operational system at the Naval Oceanographic Office on 6 March 2006, replacing the existing 1/16° system which ceased operation on 12 March 2006. Real-time and archived results are available online at http://www.ocean.nrlssc.navy.mil/global_nlom.

The 1/32° system has improvements over the earlier system that can be grouped into two categories: better resolution and representation of dynamical processes and design modifications. The design modifications are the result of accrued knowledge since the development of the earlier 1/16° system. Some of these modifications could have been implemented in the 1/16° system, but were included only in the 1/32° system because updating the 1/16° system and developing the 1/32° system concurrently wasn't feasible given manpower and computational constraints.

The improved horizontal resolution of the 1/32° system has important dynamical benefits which have implications for the model's ability to accurately nowcast and skillfully forecast. At the finer resolution, current pathways and their transport become more accurate, the global ocean circulation is changed (including inter-basin exchange) and the surface SSH variability increases and becomes more realistic. These improvements result in the 1/32° system being a better dynamical interpolator of assimilated satellite altimeter track data, using a 1-day model forecast as the first guess for the assimilation. The result is quantitatively more accurate nowcasts, as is illustrated by the model-data comparisons presented in Section 3. Based on comparisons with ocean color imagery in the northwestern Arabian Sea and the Gulf of Oman, the 1/32° system even demonstrated the capability to map small eddies, 25–75 km in diameter, with 70% reliability and a median eddy center location error of 22.5 km, a surprising and unanticipated result from the assimilation of altimeter track data. For all the eddies (50% small eddies), the reliability was 80% and the median eddy center location error was 29 km. The 1/16° system was successful for eddies > 50 km in diameter and gave a median eddy center location error of 32.5 km for the small eddies it depicted. The smallest eddies the models could realistically represent were 8×6 grid intervals in diameter or 1/4° for the 1/32° model and 1/2° for the 1/16° model at 20°N, near the middle latitude of the region used for this comparison.

The 1/32° system exhibits improved forecast skill in relation to the 1/16° system. This is due to (a) a more accurate initial condition from which to start the forecast and (b) better resolution and representation of critical dynamical processes (such as upper ocean – topographic coupling via mesoscale flow instabilities) which allow the model to more accurately evolve these features in time while running in forecast mode using forecast atmospheric forcing for the first 5 days, then gradually reverting toward climatology for the remainder of the 30-day forecast period. At 1/32° resolution forecast SSH generally compares better with unassimilated tide gauge observations and the anomaly correlation of the forecast SSH shows a larger spread when compared with persistence than the 1/16° system.

Applications for this system include assimilation and synthesis of global satellite surface data; ocean prediction; optimum track ship routing; search and rescue; anti-submarine warfare and surveillance; tactical planning; high resolution boundary conditions that are essential for even higher resolution coastal models; sea surface temperature for long range weather prediction; inputs to ice models, biochemical models and shipboard environmental products; environmental simulation and synthetic environments; observing system simulation and assessment; ocean research and education; pollution and tracer tracking; fisheries and marine resource management; impact on ocean structures such as oil rigs and inputs to water quality assessment.

The capability to map small eddies, 25–75 km in diameter, demonstrated by assimilation of altimeter data into the 1/32° model has strong implications for nested finer resolution coastal region models, including (1) the value of altimeter data for assimilation by these models and (2) the value that high resolution boundary conditions can provide them. These models should give enhanced capability in mapping small eddies, using altimeter data assimilation, over the 1/32° model due to finer resolution and to stronger topographic and atmospheric forcing constraints than found in the open ocean. However, it will be essential to separate the temporally unresolved wind-driven non-steric component of sea surface height from the altimeter data, especially in shallow water. Doing this should also benefit altimeter data assimilation into global ocean models. The separation could be done using a global high resolution, wind-driven barotropic ocean model.

Acknowledgements

6.4 projects "Large Scale Ocean Models" and "Ocean Data Assimilation" funded by SPAWAR and the Common High Performance Computing (HPC) Software Support Initiative funded project "Scalable Ocean Models with Data Assimilation". The 1/32° model results were obtained under an FY01-03 Department of Defense (DoD) HPC Challenge Project "1/32° Global Ocean Modeling and Prediction" and a grant of non-challenge computer time under the DoD HPC project "Eddy-resolving Global and Basin Scale Ocean Modeling" using the IBM SP3 (challenge) and IBM SP4 (non-challenge) at the Naval Oceanographic Office, Stennis Space Center, MS. This work includes participation in the multi-national Global Ocean Data Assimilation Experiment (GODAE) and presence on the U.S. and international steering teams. GODAE is aimed at demonstrating real-time global ocean products in a way that will promote wide utility and availability for maximum benefit to the community. The mean pathway of the Gulf Stream IR north wall used in Fig. 6 is unpublished work by Peter Cornillon and Ziv Sirkes for the ONR funded project Data Assimilation and Model Evaluation Experiment - North Atlantic Basin (DAMEE-NAB).

References

Carnes, M.R., Fox, D.N., Rhodes, R.C., Smedstad, O.M., 1996. Data assimilation in a North Pacific Ocean monitoring and prediction system. In: Malanotte-Rizzoli, P. (Ed.), Modern Approaches to Data Assimilation in Ocean Modeling, vol. 61. Elsevier, pp. 319–345.

Chassignet, E.P., Hurlburt, H.E., Smedstad, O.M., Barron, C.N., Ko, D.S., Rhodes, R.C., Shriver, J.F., Wallcraft, A.J., 2005. Assessment of data-assimilative models in the Gulf of Mexico using ocean color. In: Sturges, W., Lugo-Fernandez, A. (Eds.), New developments in the circulation of the Gulf of Mexico. Geophysical Monograph, vol. 161. American Geophysical Union, pp. 87–100.

Dietrich, G., Kalle, K., Krauss, W., Siedler, G., 1980. General Oceanography, An Introduction, 2nd ed. John Wiley. 626 pp.

Evensen, G., 1994. Sequential data assimilation with a nonlinear quasi-geostrophic model using Monte Carlo methods to forecast error statistics. J. Geophys. Res. 99, 10,143–10,162.

Fox, D.N., Teague, W.J., Barron, C.N., Carnes, M.R., Lee, C.M., 2002. The Modular Ocean Data Assimilation System (MODAS). J. Atmos. Ocean. Tech. 19, 240–252.

Hellerman, S., Rosenstein, M., 1983. Normal monthly wind stress over the world ocean with error estimates. J. Phys. Oceanogr. 13, 1093–1104.

Hogan, P.J., Hurlburt, H.E., 2000. Impact of upper ocean– topographic coupling and isopycnal outcropping in Japan/East Sea models with 1/8° to 1/64° resolution. J. Phys. Oceanogr. 30, 2535–2561.

Hogan, P.J., Hurlburt, H.E., 2005. Sensitivity of simulated circulation dynamics to the choice of wind forcing in the Japan/East Sea. Deep Sea Res. 52, 1464–1489.

Hogan, T., Rosmond, T.E., 1991. The description of the Navy Operational Global Atmospheric Prediction System's spectral forecast model. Mon. Weather Rev. 119, 1786–1815.

Holland, W.R., 1978. The role of mesoscale eddies in the general circulation. J. Phys. Oceanogr. 8, 363–392.

Holland, W.R., Lin, L.B., 1975. On the generation of mesoscale eddies and their contribution to the oceanic general circulation. I. A preliminary numerical experiment. J. Phys. Oceanogr. 5, 642–657.

Hurlburt, H.E., 1984. The potential for ocean prediction and the role of altimeter data. Mar. Geod. 8, 17–66.

Hurlburt, H.E., Hogan, P.J., 2000. Impact of 1/8° to 1/64° resolution on Gulf Stream model-data comparisons in basin-scale subtropical Atlantic Ocean models. Dyn. Atmos. Ocean. 32, 283–329.

Hurlburt, H.E., Metzger, E.J., 1998. Bifurcation of the Kuroshio Extension at the Shatsky Rise. J. Geophys. Res. 103, 7549–7566.

Hurlburt, H.E., Thompson, J.D., 1976. A numerical model of the Somali Current. J. Phys. Oceanogr. 6 (5), 646–664.

Hurlburt, H.E., Thompson, J.D., 1980. A numerical study of Loop Current intrusions and eddy shedding. J. Phys. Oceanogr. 10, 1611–1651.

Hurlburt, H.E., Fox, D.N., Metzger, E.J., 1990. Statistical inference of weakly-correlated subthermocline fields from satellite altimeter data. J. Geophys. Res. 95, 11,375–11,409.

Hurlburt, H.E., Wallcraft, A.J., Schmitz Jr., W.J., Hogan, P.J., Metzger, E.J., 1996. Dynamics of the Kuroshio/Oyashio current system using eddy-resolving models of the North Pacific Ocean. J. Geophys. Res. 101, 941–976.

Hurlburt, H.E., Rhodes, R.C., Barron, C.N., Metzger, E.J., Smedstad, O.M., Cayula, J.F., 2000. A feasibility demonstration of ocean model eddy-resolving nowcast/forecast skill using satellite altimeter data. NRL/MR/7320-00-8235. Naval Research Laboratory, Stennis Space Center, MS. 23 pp., Available on the web at http://www.ocean.nrlssc.navy.mil/global_nlom.

Jacobs, G.A., Hurlburt, H.E., Kindle, J.C., Metzger, E.J., Mitchell, J.L., Teague, W.J., Wallcraft, A.J., 1994. Decade-scale trans-Pacific propagation and warming effects of an El Niño anomaly. Nature 370, 360–363.

Jacobs, G.A., Barron, C.N., Rhodes, R.C., 2001. Mesoscale characteristics. J. Geophys. Res. 106, 19,581–19,595.

Johns, W.E., Townsend, T.L., Fratantoni, D.M., Wilson, W.D., 2002. On the Atlantic inflow into the Caribbean Sea. Deep Sea Res. 49 (2), 211–243.

Kara, A.B., Hurlburt, H.E., 2006. Daily interannual simulations of sea surface temperature and mixed layer depth using atmospherically forced OGCMs: model validation in comparison to daily buoy time series during 1980–1998. J. Mar. Syst. 62, 95–119.

Kara, A.B., Rochford, P.A., Hurlburt, H.E., 2002. Air–sea flux estimates and the 1997–1998 ENSO event. Boundary Layer Meteorol. 103, 439–458.

Kara, A.B., Wallcraft, A.J., Hurlburt, H.E., 2003. Climatological SST and MLD predictions from a global layered ocean model with an embedded mixed layer. J. Atmos. Ocean. Technol. 20, 1616–1632.

Larsen, J.C., 1992. Transport and heat flux of the Florida Current at 27°N derived from cross-stream voltages and profiling data: theory and observations. Philos. Trans. R. Soc. Lond. Ser. A: Math. Phys. Sci. 338, 169–236.

Lee, H., 1997. A Gulf Stream synthetic geoid for the TOPEX altimeter. M.S. Thesis, Rutgers University, New Brunswick, New Jersey, 36 pp.

Le Traon, P.-Y., Dibarboure, G., 1999. Mesoscale mapping capabilities of multiple-satellite altimeter missions. J. Atmos. Ocean. Technol. 16, 1208–1223.

Le Traon, P.-Y., Dibarboure, G., Ducet, N., 2001. Use of a high-resolution model to analyze the mapping capabilities of multiple-altimeter missions. J. Atmos. Ocean. Technol. 18, 1277–1288.

McPhaden, M.J., 1995. The Tropical Atmosphere Ocean (TAO) array is completed. Bull. Am. Meteorol. Soc. 76, 739–741.

Metzger, E.J., Hurlburt, H.E., 1996. Coupled dynamics of the South China Sea, the Sulu Sea and the Pacific Ocean. J. Geophys. Res. 101, 12331–12352.

Mitchell, J.L., Dastugue, J.M., Teague, W.J., Hallock, Z.R., 1990. The estimation of geoid profiles in the northwest Atlantic from simultaneous satellite altimetry and airborne expendable bathythermograph sections. J. Geophys. Res. 95, 17965–17977.

Moore, D.R., Wallcraft, A.J., 1998. Formulation of the NRL Layered Ocean Model in spherical coordinates. NRL/CR/7323-96-0005. 24pp. [Available from Naval Research Laboratory, Stennis Space Center, MS 39529-5004, USA.].

Rhines, P.B., Holland, W.R., 1979. A theoretical discussion of eddy-driven mean flows. Dyn. Atmos. Ocean. 3, 289–325.

Rosmond, T.E., Teixeira, J., Peng, M., Hogan, T.F., Pauley, R., 2002. Navy Operational Global Atmospheric Prediction System (NOGAPS): forcing for ocean models. Oceanography 15 (1), 99–108.

Shriver, J.F., Hurlburt, H.E., 1997. The contribution of the global thermohaline circulation to the Pacific to Indian Ocean throughflow via Indonesia. J. Geophys. Res. 102, 5491–5511.

Smedstad, O.M., Fox, D.N., 1994. Assimilation of altimeter data in a 2-layer primitive equation model of the Gulf Stream. J. Phys. Oceanogr. 24, 305–325.

Smedstad, O.M., Hurlburt, H.E., Metzger, E.J., Rhodes, R.C., Shriver, J.F., Wallcraft, A.J., Kara, A.B., 2003. An operational eddy-resolving 1/16° global ocean nowcast/forecast system. J. Mar. Syst. 40–41, 341–361.

Tilburg, C.E., Hurlburt, H.E., O'Brien, J.J., Shriver, J.F., 2001. The dynamics of the East Australian Current system: The Tasman Front, the East Auckland Current and the East Cape Current. J. Phys. Oceanogr. 31, 2917–2943.

Wallcraft, A.J., 1991. The Navy Layered Ocean Model users guide. NOARL Report #35. 21pp. [Available from Naval Research Laboratory, Stennis Space Center, MS 39529-5004, USA.].

Wallcraft, A.J., Moore, D.R., 1997. The NRL Layered Ocean Model. Parallel Comput. 23, 2227–2242.

Wallcraft, A.J., Kara, A.B., Hurlburt, H.E., Rochford, P.A., 2003. The NRL Layered Ocean Model (NLOM) with an embedded mixed layer sub-model: formulation and tuning. J. Atmos. Ocean. Technol. 20, 1601–1615.

Zamudio, L., Hurlburt, H.E., Metzger, E.J., Smedstad, O.M., 2002. On the evolution of coastally trapped waves generated by Hurricane Juliette along the Mexican west coast. Geophys. Res. Lett. 29 (23), 56-1–56-4.